BRILLOUIN ELASTOGRAPHY FOR PROBING BIOMECHANICAL PROPERTIES OF DISEASED TISSUES

A Dissertation

by

MARIA A. TROYANOVA-WOOD

Submitted to the Office of Graduate and Professional Studies of
Texas A&M University
in partial fulfillment of the requirements for the degree of

DOCTOR OF PHILOSOPHY

Chair of Committee,	Vladislav V. Yakovlev
Committee Members,	Philip Hemmer
	Kristen Maitland
	Alvin Yeh
Head of Department,	Mike McShane

August 2019

Major Subject: Biomedical Engineering

ABSTRACT

The overall physiological function of a tissue or organ is closely related to its mechanical properties. These properties may change during many normal physiological processes or as part of healthy adaptations to altered conditions. Outside of such routine changes, however, the healthy tissue or cell may undergo an abnormal change in mechanical properties as a result of disease or disorder. Quantifying the changes in mechanical properties can be used to deepen understanding of disease initiation and progression, or as a tool to aid diagnosis and treatment research.

Various non-destructive, non- or minimally invasive elasticity-specific imaging modalities exist that are suitable for characterization of biological material. However, they generally are suitable for evaluations on either tissue or cell level, but not both. Spatial scale matters for biomechanical characterization, as cell-level biomechanical properties do not always correspond to the mechanical properties of the corresponding tissue. In order to fully understand the underlying mechanisms of various normal and pathophysiological processes, measurements on both tissue-level and cellular level are essential. An elastography method that does not have such limitation is Brillouin elastography, or Brillouin spectroscopy, a no-contact mechanically-specific technique.

This dissertation is focused on developing and implementing a multi-modality experimental system that is capable of simultaneous Brillouin elastography, Raman spectroscopy and optional fluorescence widefield or brightfield imaging. The Brillouin spectroscopy component utilizes a tunable 532 nm excitation source, molecular iodine

absorption filter for elastically scattered light suppression, and a VIPA-based spectrometer. A novel multi-excitation Brillouin elastography approach is developed to improve SNR and correct for the distortions caused by the excessive iodine absorption, which allows to work with challenging highly-scattering samples.

Lastly, the dissertation work includes tissue-level evaluations of three different pathologies: obesity, melanoma and muscular dystrophy. The selected studies showcase the application of Brillouin spectroscopy for evaluating mechanical changes in diseased tissues.

DEDICATION

To the memory of my grandmother,

who cheered me on with steadfast support when I needed it the most

CONTRIBUTORS AND FUNDING SOURCES

Contributors

This work was supervised by a dissertation committee consisting of Professors Vladislav V. Yakovlev [advisor], Kristen Maitland and Alvin Yeh of the Department of Biomedical Engineering and Professor Philip Hemmer of the Department of Electrical and Computer Engineering.

The tissues in the obesity study in Section 4 were provided by Professor Anatoliy A. Gashev of the Department of Medical Physiology; the samples were prepared for measurements in part by Cassidy Gobbell. The tissues in the melanoma study in Section 4 were provided by Professor Duane Kraemer of the Department of Veterinary Medicine and Biomedical Sciences; the measurements were in part assisted by Dr. Zhaokai Meng. The live *Drosophila* larvae in the muscular dystrophy study in Section 4 were provided by Professor Vladislav M. Panin of the Department of Biochemistry and Biophysics; the larvae were maintained and prepared for measurements by Ishita Chandel.

All other work conducted for the dissertation was completed by the student independently.

Funding Sources

Graduate study was supported by Consortium Research Fellows Program (CRFP) fellowship in partnership with Air Force Research Laboratory, P.E.O. Scholar Award from P.E.O. International, Optics and Photonics Education Scholarship from SPIE, and Graduate Diversity Fellowship from Texas A&M University.

This work was also made possible in part by National Science Foundation (NSF) (DBI-1455671, DBI-1532188, ECCS-1509268, CMMI- 1826078); Air Force Office of Scientific Research (AFOSR) (FA9550-15-1-0517, FA9550- 18-1-0141); Defense Advanced Research Projects Agency (DARPA) (FA8650-13-D- 6368/0006); Office of Naval Research (ONR) (N00014-16-1-2578); National Institute of General Medical Sciences (NIGMS) (1R01GM127696-01); National Institutes of Health (DK099161); U.S. Department of Defense (FA9550-15-1-0517) and Cancer Prevention Research Institute of Texas (RP160834).

TABLE OF CONTENTS

Page

LIST OF FIGURES

Page

Page

Page

1. INTRODUCTION

1.1 Biomechanical properties: background and significance

Biomechanical properties characterize the response of an investigated organ, tissue, cell or other biological material to an application of external force. The overall physiological function of a tissue or organ is closely related to its mechanical properties. Common examples of this relationship are locomotion function of skeletal muscle, structural support of bones and mechanical protection provided by adipose tissue.

Changes in tissues' or cells' mechanical properties correlate with the progression of many normal physiological processes or adaptations to environment change, such as embryonic development [1], bone healing [2] and high-altitude lung acclimatization [3]. These changes can act both as an indicator of the adjustment and as a driving force guiding the normal physiological process. Outside of normal processes or adaptations, mechanical properties may undergo an abnormal change from the parameters of healthy tissue as a result of disease or disorder. Osteoporosis [4], osteoarthritis [5], presbyopia [6], pulmonary fibrosis [7], Duchenne muscular dystrophy [8,9] and various cancer types [10–12] are among the many afflictions that alter the mechanical properties of the affected tissues.

Quantification of the changes in the mechanical properties of tissues and cells makes it possible to evaluate the progression of normal or abnormal processes or locate the margin of the affected tissue. This knowledge can be used to improve diagnosis and

early detection, as well as aid treatment research through a greater understanding of the processes driving various diseases.

1.2 Overview of current elastography techniques

Biological tissues and cells are considered viscoelastic, possessing in various degrees both elasticity and viscosity, or the resistance to deformation and flow respectively. Various non-destructive, non- or minimally invasive elasticity-specific imaging modalities exist that are suitable for characterization of biological material. Among them are magnetic resonance elastography (MRE), ultrasound (US) elastography, optical coherence elastography (OCE), photoacoustic elastography (PAE) and atomic force microscopy (AFM) elastography. The approximate relative resolution ranges of these techniques are shown in Figure 1.1. Some techniques are ideal for investigations in cell culture, while others are more suited for bulk tissue studies.

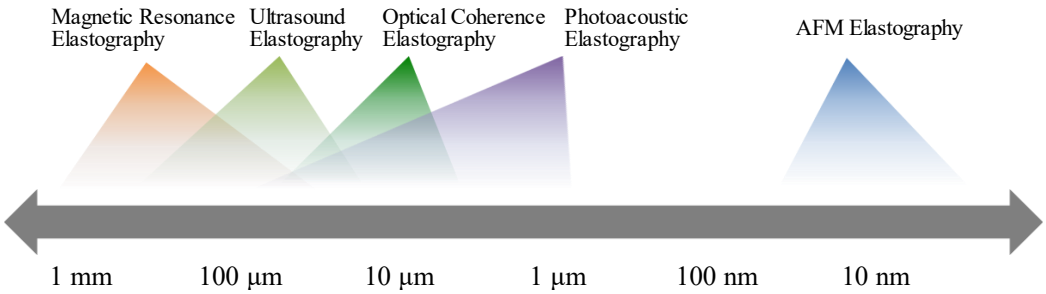

Figure 1.1 Relative resolutions of various elastography techniques.

1.2.1. Magnetic resonance elastography (MRE)

Magnetic resonance elastography (MRE) [13] employs a modified phase-contrast magnetic resonance imaging (MRI) sequence to visualize propagating transverse shear

waves that are produced in the sample by a pneumatic, electromechanical or other actuator. The final elastograms, quantitative maps of tissue stiffness, are then produced using post-processing inversion algorithms. The MRE is suitable for investigation of mechanical properties in whole organs and large parts of the body and is routinely used in clinical setting; however, it is not suitable for studies of tissue microstructure.

1.2.2. Ultrasound (US) elastography

Ultrasound (US) elastography [14] measures the changes in the recorded ultrasound echoes as the sample undergoes some mechanical stimulation (for example, a pressure applied by a transducer). The results are then compared to the pre-compression measurements, and the elasticity score of the sample is calculated. The best resolution is achieved by using a higher frequency; however, in such systems the increased attenuation of the acoustic wave greatly reduces the imaging depth [15]. The US elastography is a non-invasive method suitable for studies using bulk biological tissues, but it does not have a spatial resolution sufficient for evaluation of tissue microstructure or cell investigations.

1.2.3. Optical coherence elastography (OCE)

Optical coherence elastography (OCE) [16,17], sometimes referred to as optical coherence tomography (OCT) elastography, assesses tissue's mechanical response through OCT measurements, an interferometric imaging modality. Like many other elastography techniques, OCE generally relies on an application of external load or stimulation. This non-invasive elastography technique produces high resolution images of biological tissue microstructure, but is not suitable for single cell investigations.

1.2.4. Photoacoustic elastography (PAE)

Photoacoustic (PA) elastography (PAE) [18,19] is an elastography technique based on PA tomography (PAT)/PA computed tomography (PACT) or PA microscopy (PAM) imaging modalities. The PA imaging techniques are based on the PA effect, in which the absorption of light is followed by a temperature increase that induces a pressure rise, which propagates as a PA wave. Via the acoustic detection, an image of optical absorption contrast is created with high resolution and penetration. In PAE, images of the sample are taken before and during application of external force (such as compression plate), and then cross-correlated to calculate the displacement of the light absorbing targets, yielding a strain image. PAE is an elastography method that is well-suited for non-invasive investigations in both biological tissues (PAT/PACT-based PAE) and cells (PAM-based PAE). However, the need to match the excitation wavelength to the strong endogenous absorbers in the tissue of interest puts a limitation on the broad use of the technique. To fully evaluate the mechanical properties of inhomogeneous tissue, several excitation sources may be required targeting different strong absorbers.

1.2.5. Atomic force microscopy (AFM) elastography

Elasticity measurements of a single cell can be achieved using atomic-force microscopy (AFM) elastography [20]. A typical AFM apparatus consists of a sharp tip mounted on a flexible cantilever, a laser source that is focused on the back of it, and a photodetector. As the sharp tip is scanned over a sample's surface, the tip-surface forces result in bending of the cantilever. This vertical movement causes changes in the reflected laser's spot position, which are then translated into an image of the sample's surface. The

sharp tip can also be used as an indenter for measuring the elastic response of the sample to an applied pressure.

AFM elastography has an ultra-fine spatial resolution on the order of nanometers, but a very limited field-of-view (FOV). This imaging method is commonly applied to investigate live cells or *ex vivo* tissue components, such as cartilage. The FOV of AFM is much smaller than the size of a cell, diameter of which ranges in 1-100 μm. Imaging the elasticity of an individual cell is a time-consuming process and AFM elastography is unsuitable for bulk tissue applications.

1.3 Significance of mechanical assessment on different spatial scales

Cell-level biomechanical properties do not always correspond to the mechanical properties of the corresponding tissue; a common example of this disparity is cancer. On tissue level, cancer lesions are often stiffer than the surrounding healthy tissue [10–12]. Cells within the tumor sense the increased rigidity of their microenvironment [21,22], and alter their cytoarchitecture and motor protein activity to withstand the increased compressive forces [22–24]. The individual cancer cells then become softer than the corresponding normal cells [25], a change that is related to malignant cells' ability to invade and metastasize [26,27].

Spatial scale matters for biomechanical characterization, however, the above-reviewed elastography methods reveal a gap in the imaging scales between OCE and AFM elastography. In order to fully understand the underlying mechanisms of various normal and pathophysiological processes, measurements on both tissue-level and cellular level are essential.

One of the described techniques, PAE, bridges this gap, as PAT-based elastography is suitable for investigations of whole organs and PAM-based method can achieve sub-micron resolution. However, this technique requires use of a broadly tunable or multiple light sources to match multiple target absorbers in different samples and relies on external or internal mechanical stimulation for the mechanical response assessment. A different elastography technique exists that spans the gap in the imaging scales and does not have these limitations – namely, Brillouin elastography.

Brillouin elastography, or Brillouin spectroscopy, is a truly no-contact mechanically-specific imaging modality that is suitable for investigations in both bulk tissue and individual cells. This optical technique can be used to probe viscoelastic properties of the material and is based on Brillouin scattering, a type of inelastic scattering. Spontaneous Brillouin elastography does not require application of mechanical stimulation as the Brillouin scattering phenomenon occurs upon interaction of the incident photons with spontaneous, or thermal, acoustic phonons of the material. Additionally, the same excitation source can be used for a variety of different tissues and cell culture samples.

1.4 Brillouin elastography

1.4.1. Spontaneous Brillouin scattering

Spontaneous Brillouin scattering occurs when light is inelastically scattered by density fluctuations due to thermal vibrations of media's atoms and molecules about their equilibrium positions. The thermal density fluctuations propagate in the media in all possible directions and lead to periodic local variations of the refractive index. These

periodic fluctuations can be viewed as a Bragg grating with a period of Λ – the wavelength of the elastic or acoustic wave – traveling in the media at hypersound velocity V_s (Figure 1.2, a). Since the acoustic velocity is at least four-five orders of magnitude smaller than the speed of light, the grating can be considered quasi-static, or "frozen" in time. The parallel planes of higher refractive index will each partially reflect the incident light (Figure 1.2, b) if the angle of incidence θ_i satisfies the Bragg condition for constructive interference:

$$\sin\theta_i = \frac{\lambda_0}{2n\Lambda} \qquad \textbf{1.1}$$

where λ_0 is the wavelength of the incident light, n is the refractive index and Λ is the period of the refractive index variations (the wavelength of the acoustic wave).

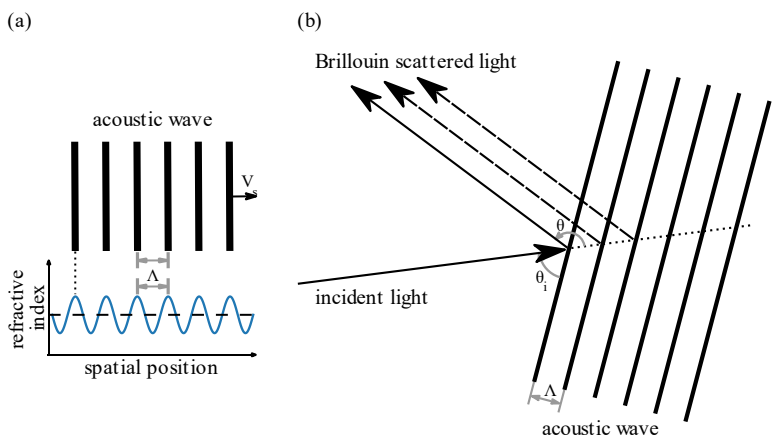

Figure 1.2 (a) Periodic local variations of the refractive index viewed as Bragg grating traveling with velocity of sound; (b) Spontaneous Brillouin scattering process: the incident light undergoes multiple reflections from elastic wave propagating in the medium viewed as a quasi-static event.

Rewriting equation 1.1 in terms of the scattering angle θ, the angle between the propagation direction of the scattered (reflected) and incident waves, yields:

$$\sin\frac{\theta}{2} = \frac{\lambda_0}{2n\Lambda} \qquad \textbf{1.2}$$

from where we can obtain the frequency of the acoustic wave ν_s using relation $\Lambda = V_s/\nu_s$:

$$\nu_s = \frac{2nV_s}{\lambda_0}\sin\frac{\theta}{2} \qquad \textbf{1.3}$$

As the Bragg grating is moving in the media with velocity V_s, the reflection of the incident monochromatic wave will be accompanied, as a result of the Doppler effect, by a frequency shift equal to the frequency of the acoustic wave. This frequency shift is the Brillouin shift, $\Delta\nu_B$:

$$\Delta\nu_B = \pm\frac{2nV_s}{\lambda_0}\sin\frac{\theta}{2} \qquad \textbf{1.4}$$

Equation 1.4 is the mathematical representation of frequency shift from the frequency of the incident light due to Brillouin scattering. The positive and negative signs correspond to the acoustic wave's propagation direction and represent anti-Stokes and Stokes shifts. From quantum mechanical point of view, Brillouin scattering occurs due to interaction of the incident photon with acoustic phonon, a quantum of vibrational mechanical energy associated with the elastic wave. This interaction results in the photon transferring energy to or acquiring energy from the acoustic phonon, yielding Stokes or anti-Stokes shifts in frequency.

The Brillouin spectrum, therefore, consists of a doublet of peaks symmetrically positioned in close proximity around the Rayleigh peak in the center (Figure 1.3). The

Rayleigh peak has no frequency shift and is caused by elastic scattering from non-propagating density fluctuations. The Brillouin peaks, on the other hand, occur due to inelastic scattering from density fluctuations propagating at hypersound velocity, resulting in a small frequency shift, typically on the order of 1-20 GHz (~1-20 pm). For comparison, Figure 1.3 also shows Raman peaks (displayed as single Stokes and anti-Stokes peaks for clarity), that occur due to inelastic Raman scattering determined by vibrational and rotational frequencies of the atoms and molecules of the media. Frequency shifts due to Raman scattering are comparable to optical frequency, typically on the order of 1-100 THz (~10-3000 cm^{-1} or 1-100 nm), and lay further from Rayleigh peak than the Brillouin peaks.

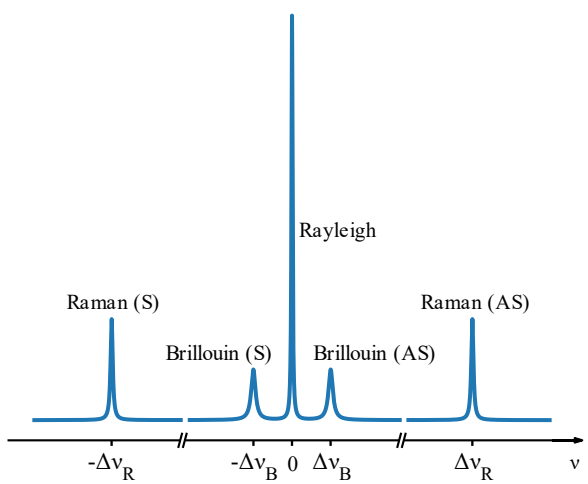

Figure 1.3 Example spectrum: relative positions of peaks due to Rayleigh, Brillouin and Raman scattering processes.

As the acoustic wave propagates in the media in all possible directions, the Brillouin frequency shift has a longitudinal and two transverse (shear) components. The components can be probed selectively by changing the collection geometry. The

longitudinal component is obtained by limiting the collection to backscattered light (θ = 180°), which is also the maximum possible Brillouin shift value, as seen from equation 1.4:

$$\Delta \nu_{B_{MAX}} = \pm \frac{2nV_s}{\lambda_0} \qquad \textbf{1.5}$$

The microscope objective lens is used to focus the incident light onto the sample and to collect the backscattered signal. The finite NA objective lenses used for excitation and signal collection contribute to a spectral broadening of the Brillouin peaks, which is more pronounced when using high NA objectives (NA>0.5). A lower NA objective limits this spectral broadening at a sacrifice of the spatial resolution. The NA=0.5 objective lens used in the studies included in this dissertation causes insignificant broadening due to the 180° signal collection angle. The backscattering geometry results in a less pronounced spectral broadening, compared to a 90° collection angle. [28] Additionally, due to backscattered collection geometry, such measurements of Brillouin scattering contain mainly contribution from longitudinal wave, and not the shear (transverse) waves. [29]

The acoustic wave decays as it travels through the media due to viscous dampening mechanisms, resulting in frequency broadening of the Brillouin scattering. The attenuation coefficient of the acoustic wave, μ, is expressed as

$$\mu = \frac{2\Gamma \Delta \nu_B^2}{V_s} \qquad \textbf{1.6}$$

where $\Gamma = \eta/\rho$ is the damping parameter, η is the viscosity and ρ is the density of the media.

This frequency broadening results in broadening of the Brillouin peaks, the full width at half maximum (*FWHM*) value of which is proportional to the attenuation coefficient:

$$FWHM_{\Delta\nu_B} = \frac{\mu V_s}{\pi} \qquad \textbf{1.7}$$

1.4.2. Mechanical characterization with Brillouin elastography

Mechanical properties of the material characterize the response it exhibits upon application of external force; among them are elasticity and viscosity. Elasticity is a property of a material to resist the deformation due to the external force, the original shape of the material is regained after the force is removed. Viscosity, on the other hand, is the measure of the material's resistance to flow. Materials that have characteristics of both elasticity and viscosity are called viscoelastic. Biological tissues are viscoelastic, and they exhibit viscoelastic behavior to a different extent, depending on the tissue's composition and structure.

Most conventional approaches to obtain information on mechanical properties involve measuring the material's response to an applied force. However, the standard methods are invasive, potentially destructive, have poor spatial resolution, and are not suitable for biological samples. Various non-destructive, non- or minimally invasive elasticity-specific imaging modalities exist that are capable of evaluating stiffness of biological tissues. Among them are ultrasound (US) elastography, magnetic resonance elastography (MRE), optical coherence elastography (OCE), atomic force microscopy (AFM) elastography and, gaining popularity in recent years, Brillouin spectroscopy or elastography.

Since the spontaneous Brillouin scattering occurs due to the interaction of the incident light with the spontaneous thermally induced acoustic waves within the sample, mechanical characterization using Brillouin spectroscopy is obtained in a non-invasive manner, non-destructive and label-free – making it an attractive technique for investigation of biological materials. Mechanical characterization using Brillouin spectroscopy has been successfully performed in inorganic material characterization [30], remote sensing [31], and biomedical applications [32–35], including elasticity-mapping of a single cell [36,37]. Brillouin spectroscopy nondestructively measures the local elasticity and viscoelasticity with high spatial resolution and is suitable for both bulk tissue and individual cells. Additionally, Brillouin spectroscopy can be combined with another inelastic-scattering based technique, Raman spectroscopy, to simultaneously obtain information of the chemical compositions of the investigated material.

The Brillouin scattering phenomenon is associated with the longitudinal acoustic waves propagating in the material. From the differential equation describing the propagation of a longitudinal acoustic wave in viscoelastic medium, the complex longitudinal modulus M can be derived as [38]

$$M = M' + iM'', \qquad \textbf{1.8}$$

where

$$M' = \rho V_s^2 \qquad \textbf{1.9}$$

and

$$M'' = \frac{\rho V_s^2 FWHM_{\Delta\nu_B}}{\Delta\nu_B} \qquad \textbf{1.10}$$

The real part of the complex longitudinal modulus, M', referred to as "storage modulus," yields information on the elastic behavior of the material. In the Brillouin spectrum, the real part of the complex longitudinal modulus corresponds to the Brillouin shift – the position of the Brillouin peak relative to the unshifted Rayleigh frequency. Combining equations 1.4 and 1.9 and assuming backscattering collection geometry yields an expression relating the longitudinal storage modulus, sometimes referred to as high-frequency elastic modulus or Brillouin modulus, to the value of the Brillouin frequency shift:

$$M' = \frac{1}{4}\rho\left(\frac{\Delta\nu_B\lambda_0}{n}\right)^2 \qquad \textbf{1.11}$$

The imaginary part of the complex longitudinal modulus, M'', the "loss modulus," provides information on the acoustic attenuation of the sample, describing the material's viscous response. In the Brillouin spectrum, the imaginary part of the complex longitudinal modulus corresponds to the natural or corrected linewidth of the Brillouin peak – the FWHM after accounting for the broadening of the recorded peak due to NA of the objective lens, finite resolution of the spectrometer and the contributions from multiple components in inhomogeneous material. Assuming backscattered collection geometry, equations 1.4, 1.6, 1.10 and $\Gamma = \eta/\rho$, we can obtain analytical expression for the viscosity η and the loss modulus M'':

$$\eta = \frac{\rho \pi FWHM_{\Delta \nu_B}}{2\Delta \nu_B^2} \qquad \textbf{1.12}$$

and

$$M'' = \frac{\rho \lambda_0^2 \Delta \nu_B FWHM_{\Delta \nu_B}}{4n^2} \qquad \textbf{1.13}$$

2. INSTRUMENTATION

2.1 Challenges in practical application of Brillouin elastography

Brillouin elastography, or Brillouin spectroscopy, is a powerful technique that can be used to non-invasively characterize the mechanical properties of biological and inorganic material on both microscopic and macroscopic scales. However, the small difference in frequency between Brillouin- and elastically-scattered peaks, coupled with the elastically scattered light being several orders of magnitude higher in intensity, makes practical application of Brillouin spectroscopy challenging.

Multiple approaches exist to suppress or eliminate the strong elastically scattered light that can make it impossible to distinguish the smaller Brillouin peaks in the collected spectrum. Among the common strategies to suppress the elastically-scattered light with no or minimal attenuation of the Brillouin signal are multi-stage virtually imaged phase array (VIPA) [39], Fabry-Perot etalon [40,41] and molecular or atomic absorption-based ultra-narrow notch filter [42,43]. In the presented dissertation work, an absorption-based filter is used in the form of iodine vapor-filled quartz cuvette placed in a temperature-adjustable heated mount. More discussion on the use of absorption-based filter for elastic scattering suppression is given in Subsection 2.1.1, page 16.

Similarly to suppression of elastically scattered light, a number of strategies are utilized to spectrally resolve Brillouin and Rayleigh peaks. Since the frequency shift of Brillouin-scattered light is very small, conventional grating-based spectrometers (typical resolution of 20-500 pm) do not possess sufficient resolution to accurately measure the

Brillouin shift, which is on the order of 1-20 GHz, or approximately 1-20 pm. Common methods to acquire Brillouin measurements and measure the value of the Brillouin shift are based on scanning multi-stage Fabry-Perot interferometer and VIPA spectrometer. The work described in this dissertation uses home-built VIPA-based spectrometer, which typically requires shorter acquisition times than scanning or non-scanning Fabry-Perot interferometers while providing sufficient spectral resolution for applications of Brillouin spectroscopy [44–46]. More information of the structure and operation of the VIPA and its use as a wavelength dispersion device is provided in Subsection 2.1.2, page 18.

2.1.1. Iodine absorption ultra-narrow notch filter

Using molecular or atomic absorption as an ultra-narrow notch filter provides consistent suppression of the elastically-scattered light that would otherwise obscure the weak Brillouin signal. The system designed as part of the dissertation work is based around a 532 nm excitation source, making iodine a suitable choice for the absorption filter. Adjusting the temperature of the iodine vapor-filled cuvette changes the optical density of the vapor, providing control over the degree of suppression.

Ideally, the temperature is carefully selected for suppression that is sufficiently high to detect the small Brillouin peaks while not so high that it distorts the baseline of the collected spectrum or alters the shape of the Brillouin peaks. To overcome this limitation, a novel multi-excitation Brillouin elastography approach was developed as part of the dissertation work, described in Section 3, page 24, that allows for reconstruction of the Brillouin spectrum from distorted signal.

The use of absorption notch filter requires that the emission of the excitation laser matches a strong absorption band, and that it experiences no spectral drift. A possible approach, such as utilized in this dissertation work, is the use of a stable tunable 1064 nm laser with MgO:PPLN crystal for the second harmonic generation of 532 nm excitation that is tunable in the ± 20 GHz range.

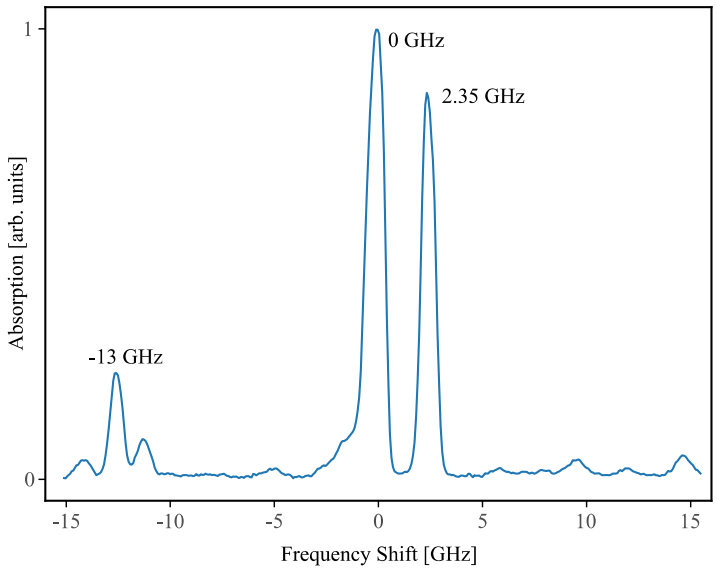

Figure 2.1 Iodine absorption spectrum in the region of the selected excitation wavelength, 0 GHz corresponds to the excitation wavelength.

Molecular iodine has many absorption bands within the tunable range of the excitation source [47], however, few of them are positioned at a sufficient distance from another strong absorption band. The selected region, shown in Figure 2.1, was chosen for its strong main absorption band (line 638), and convenient spacing to the closest bands: a secondary absorption band (line 637) at a distance of 2.35 GHz and a significantly weaker absorption band at a distance of approximately 13 GHz. It was experimentally determined

that the secondary absorption bands have small negative effect on the quality of the final Brillouin spectra. For especially challenging samples with high scattering the adverse effects are more notable, but a “pure” spectrum can be reconstructed from the distorted signal using the multiple-excitation Brillouin spectroscopy approach (see Section 3 for more detail).

2.1.2. Virtually imaged phase array (VIPA)-based spectrometer

The virtually imaged phase array (VIPA) is an interferometric wavelength dispersion device with high spectral dispersion. The device can be described as a tilted etalon with a side entrance window. The VIPA consists of two parallel flat reflective surfaces: a total reflector with a transparent entrance window at the front and a partial reflector at the back surface. The collimated incident light enters the device through the transparent entrance window at an angle close to normal incidence, which ensures a large number of internal round-trip reflections between the two surfaces.

Figure 2.2, (a) shows a simplified diagram of VIPA that, for clarity, ignores refraction at the front and back interfaces between air and VIPA substrate, such as fused silica. A cylindrical lens (not shown) placed before the VIPA line-focuses the input light onto the back partial reflector surface, after which the input beam undergoes many round-trip reflections. Each time the beam is reflected from the partial reflector surface, some small portion exits the VIPA. Each beam in the resultant series of displaced beams appears as if the light diverges from a virtual image of the line focus. The virtual sources are equally spaced $2t$ apart progressively further away from the VIPA, where t is the thickness of the VIPA.

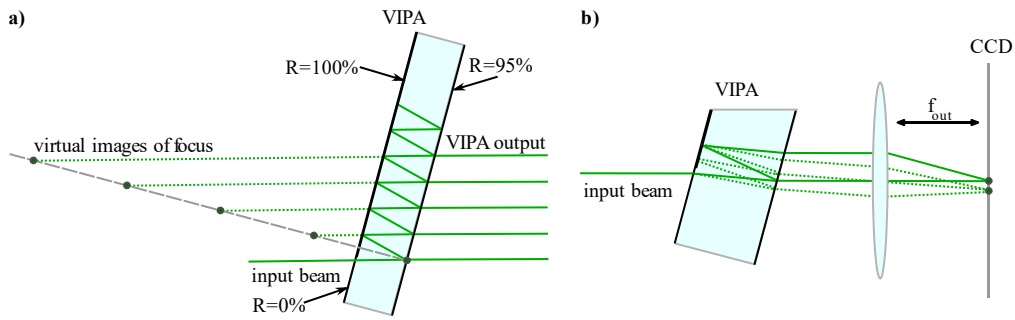

Figure 2.2 (a) Simplified structure and operation of VIPA (refraction at front and back surfaces ignored for clarity) and (b) Detail of VIPA's angular wavelength dispersion showing separation of two different wavelengths (angular dispersion is exaggerated for clarity).

After exiting the device, the interference between optical beams resulting from different number of round trips, or virtual sources, produces collimated light with high angular dispersion (Figure 2.2, (b)). The output of the VIPA is focused with a spherical lens onto the detector to spatially disperse different wavelengths. The intensity at the detector is given by [48]:

$$I_{out}\left(x_F,\lambda\right) \propto \left|E_{out}\left(x_F,\lambda\right)\right|^2 \propto \exp\left(-\frac{2 f_{in}^2 x_F^2}{f_{out}^2 W^2}\right)\frac{1}{\left(1-R_f R_b\right)^2 + 4\left(R_f R_b\right)\sin\left(\frac{k\Delta}{2}\right)} \qquad \textbf{2.1}$$

where: x_F is the position along the x-axis of the output lens focal plane,

λ and W are the wavelength and beam diameter of the input light,

f_{in} and f_{out} are the focal lengths of the input and output lenses respectively,

R_f and R_b is the reflectivity of the front and back surfaces respectively,

$k = \frac{2\pi}{\lambda}$,

$$\Delta = 2t\cos(\theta_i) - \frac{2t\sin(\theta_i)x_F}{f_{out}} - \frac{t\cos(\theta_i)x_F^2}{f_{out}^2} \text{ and}$$

t is the thickness of the VIPA.

2.2 General description of the optical system

2.2.1. The original optical system

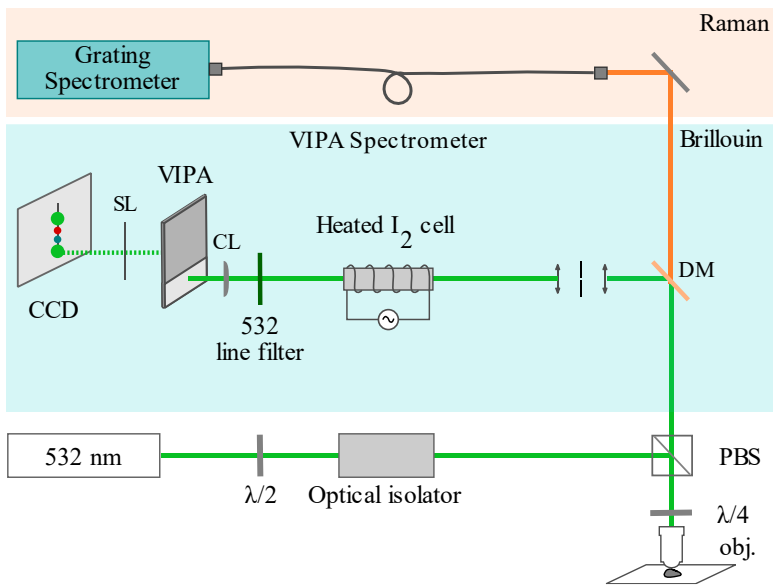

Figure 2.3 The original optical system for simultaneous Brillouin and Raman spectroscopy.

The original optical system available at the beginning of this dissertation research was designed and implemented by Dr. Zhaokai Meng [49]. That starting system, shown in Figure 2.3, was capable of simultaneous Brillouin and Raman spectroscopy and did not, at the time, have other imaging capabilities. The original system utilized a single-mode solid-state 532 nm laser as an excitation source, a single-pass heated iodine vapor-filled

cuvette as ultra-narrowband notch filter of elastically scattered light and a VIPA-based Brillouin spectrometer.

In order to optimize the optical system for work with a wide range of biological samples, several major areas for improvement were identified:

- insufficient suppression of elastically scattered light
- spectral drift of the 532 nm laser, leading to
    - drifting out of I_2 absorption band, rendering the molecular notch filter inoperative
    - inconsistent spectra, even when acquired only minutes apart, making data analysis automation unreliable
- lack of brightfield imaging for sample positioning
- lack of fluorescence imaging for work with fluorophore-labeled samples

2.2.2. The improved optical system

As a part of the dissertation work, the original optical system has been heavily modified over time. The end result provides a greater reliability, repeatability and suitability for biological samples over the original system. The final multi-modality system (Figure 2.4) includes components for simultaneous Brillouin elastography, Raman spectroscopy and optional fluorescence widefield or brightfield imaging, which share the detector. Depending on the fluorophore of interest, fluorescence imaging and Brillouin elastography cannot be used simultaneously.

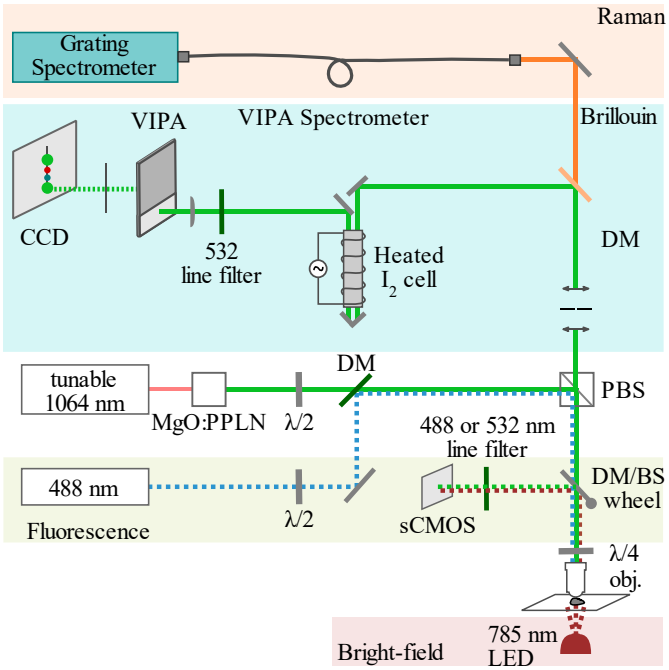

Figure 2.4 The improved optical system for simultaneous Brillouin elastography, Raman spectroscopy and optional fluorescence widefield imaging or brightfield imaging.

The major change in the improved experimental system is the use of a tunable 532 nm excitation source, which is achieved via frequency doubling (second harmonic generation, SHG) of a tunable continuous-wave 1064 nm laser source. The wavelength of the seed laser is set to match a strong absorption band of iodine (line 638 [47], around -139.8 pm offset from the central wavelength of the 1064 nm seed diode laser, as it is defined by the manufacturer (Koheras Adjustik Y10, NKT Photonics, Inc.), which serves as an ultra-narrowband notch filter of elastically scattered light [50]. A stable, tunable excitation source not only ensures a reliable suppression of elastically scattered light, but also provides repeatability of measurements. The implemented change in the laser source

allowed automation of data processing and the use of reference sample to calibrate or set the x-axis of the spectra.

The performance of the implemented VIPA-based Brillouin spectrometer with the described tunable excitation source is characterized in Reference [51]. Briefly, the implemented VIPA-based system was compared to a tandem 6-pass Fabry-Perot interferometer system with two different 532 nm excitation sources. The VIPA-based system displayed higher stability, with calculated Brillouin shift deviation of under 8 MHz from the median values acquired with exposures from 0.512 to 102.4 s. It also proved to have superior sensitivity, with the power at the sample required to resolve the Brillouin peaks at 0.512 s of 0.8 mW, compared to 29-30 mW requirement of the other system.

Other changes to the optical system include double-passing of the collected light through the iodine cuvette. This change, together with matching the excitation wavelength to the absorption band of molecular filter, provides greater suppression of the elastically scattered light. Additionally, fluorescence widefield imaging was implemented using solid-state 488 nm excitation source co-aligned with the incident 532 nm beam. Lastly, brightfield imaging using 785 nm LED light source (M785L3, Thorlabs, Inc.) was added in trans-illumination configuration.

3. MULTI-EXCITATION BRILLOUIN SPECTROSCOPY*

The current section describes a recently developed approach to correct the undesired background distortions in the Brillouin spectra caused by molecular filter's absorption, fluorescent emission, ambient room light or other constant contaminant. Due to the weak intensity of the Brillouin signal, a distortion of the baseline or a partial absorption of Brillouin peak can have strong impact on data analysis. In the worst case, such as investigation of strongly scattering biological material with simultaneous fluorescence measurements, these perturbations can make it impossible to accurately determine the Brillouin shift.

The developed multi-excitation Brillouin spectroscopy method computationally reconstructs the pure Brillouin signal component from multiple Brillouin spectra acquired using different excitation wavelengths, allowing Brillouin elastography measurements from more challenging samples. The scientific premise for this method is based on the fact that the position of the peaks of Brillouin and elastically scattered light is dependent on the excitation wavelength. On the other hand, baseline distortions due to molecular filter absorption, ambient light or simultaneous fluorescence imaging remain unchanged with varying incident wavelength.

---

* Part of this section is adapted with permission from "Sequentially-Shifted Excitation (SSE) Brillouin spectroscopy for recovering signal contaminated with strong scattering, absorption or fluorescence," by M. Troyanova-Wood and V.V. Yakovlev, *Proc. SPIE 10880*, Optical Elastography and Tissue Biomechanics VI, 1088016 (5 March 2019) (Reference [61])

The principle behind the method is first explained on a set of Raman spectra of solution of DMSO and fluorescent dye, then illustrated on a set of simulated Brillouin spectra with excessive absorption. Next, an experimental application of multi-excitation Brillouin spectroscopy is given on measurements of cream, a highly-scattering sample, the recorded Brillouin spectra of which are strongly distorted by excessive iodine absorption.

3.1 Motivation

Brillouin elastography has been picking up steam in the last several years [52,53], with an increasing number of various applications of the technique [43,54–60], especially on easier to work with transparent and semi-transparent samples. However, it is only fairly recently that studies started focusing on improving the SNR of the resultant spectra, enabling work with more challenging turbid samples. The present section of the dissertation reports the recently developed method for correction of Brillouin data distorted by excessive absorption of the molecular filter – multi-excitation Brillouin spectroscopy.

Among the most challenging aspects of Brillouin spectroscopy is the closeness of Brillouin and Rayleigh-scattering spectral peaks as well as the weakness of the Brillouin signal. A number of approaches exist that address resolving the Brillouin and elastic peaks, based mainly on Fabry-Perot interferometer and virtually imaged phase array (VIPA). Similarly, a number of methods exist that eliminate or partially suppress the elastically scattered light that can completely obscure the Brillouin peaks. Common methods are

multi-stage VIPA [39], Fabry-Perot etalon [40,41] and molecular or atomic absorption-based ultra-narrow notch filter [42,43].

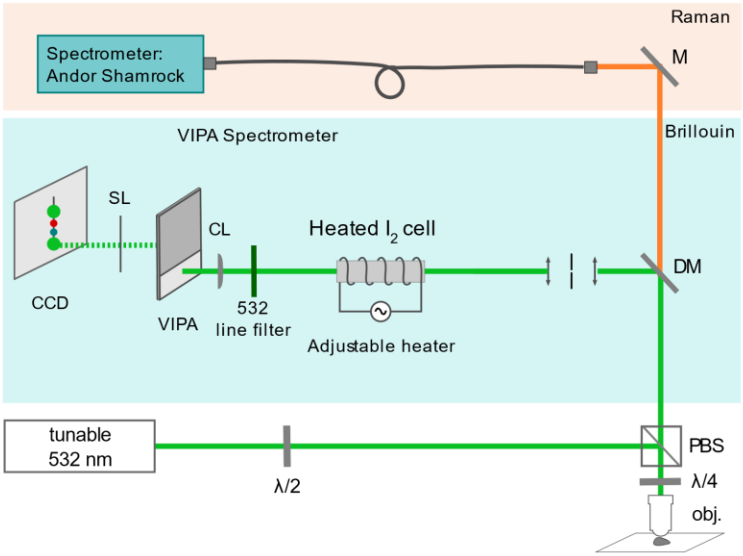

Figure 3.1 A simplified schematic diagram of instrumental setup for Brillouin spectroscopy. Features of interest are tunable 532 nm single-wavelength laser source, iodine-filled heated cuvette for elastic scattering suppression and VIPA spectrometer.

The approach implemented by the Yakovlev's group at Texas A&M University is a single-stage VIPA spectrometer and a molecular filter for suppression of the elastically scattered light (see Figure 3.1 for the schematic diagram of the optical setup). The system utilizes a tunable 532 nm excitation light source (Section 2.2.2, p. 21) that is set to match a strong absorption band of iodine vapor in a heated quartz cuvette. Matching the wavelength of the excitation light to the absorption of iodine (or other vapor for a source of different wavelength) ensures that the strong elastically-scattered light does not obscure the weak Brillouin signal. However, while the undesired elastically-scattered signal is significantly reduced, careless selection of the excitation source (wavelength mismatch or

spectral drift over time) or too high of optical density of the filter can lead to loss of signal quality. Setting the temperature of the iodine-filled cuvette too high may result in suppression of one of the Brillouin peaks or distortion of the Brillouin spectra's baseline/background. These distortions not only reduce the quality of the obtained signal, but can make curve fitting of the peaks difficult, producing an error in the value of the measured Brillouin shift.

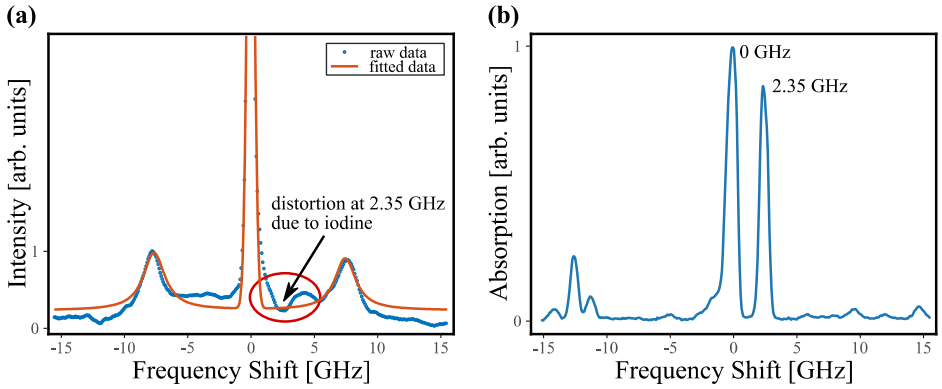

Figure 3.2 a) Brillouin spectrum of Drosophila larva muscle, arrow indicates slight baseline distortion caused by iodine absorption. Stronger distortion in highly-scattering samples can affect the Lorentzian fitting of Brillouin peaks. b) Iodine absorption in the region of the excitation wavelength. The smaller band at 2.35 GHz is the cause of the distortion in part a).

The method described in the current section was originally designed to correct for a mild distortion of the signal baseline that is typically present when working with highly scattering samples, such as the Brillouin spectrum of *Drosophila* larva's muscle in Figure 3.2a, marked with an arrow. Comparing the Brillouin spectrum to the measured absorption spectrum of iodine in the region centered at the selected excitation wavelength (Figure 3.2b), this small distortion was determined to be caused by the secondary absorption band

at around 2.35 GHz. While insignificant in most samples, the distortion of the baseline can prove problematic for automated data processing for low SNR spectra due to poor or failed curve-fitting of the Brillouin peaks. Aside from distortions caused by excessive absorption, the multi-excitation Brillouin spectroscopy method can be utilized to improve the SNR of spectra with weak Brillouin signal and correct for background caused by ambient light or simultaneous fluorescence imaging.

The dissertation describes a novel modification of Brillouin spectroscopy, the multi-excitation Brillouin spectroscopy, previously referred to as Sequentially-Shifted Excitation (SSE) Brillouin spectroscopy (Reference [61]) when limited to constant change in excitation wavelength value. The technique consists of computationally reconstructing Brillouin signal from multiple spectra acquired using different excitation wavelengths. Multi-excitation Brillouin spectroscopy is capable of reconstructing the Brillouin peaks from even the most distorted spectra, eliminating the effects of molecular filter's excessive absorption, ambient light and emission from simultaneous fluorescence imaging, greatly improving the SNR of the spectrum and improving the results of further data processing.

3.2 Principle

Removal of undesired distortions of the signal is not a new problem, and many techniques exist for baseline correction in Raman spectroscopy [62]. Among the most common approaches for removal of fluorescent background is fitting the baseline to a polynomial function and subtracting it from the spectrum. Such an approach can be applied to Brillouin spectroscopy for cleanup of weak fluorescence or other simple baseline, but is not suitable for removal of the distortion caused by the molecular filter's

excessive absorption. In Raman spectroscopy, some background removal approaches are based on the use of different excitation wavelengths, such as commonly-used shifted excitation Raman difference spectroscopy (SERDS), multi-excitation Raman spectroscopy [63] and its modification, the Sequentially-Shifted Excitation (SSE) Raman spectroscopy [64]. This subsection describes the concepts of multi-excitation reconstruction for use in Brillouin spectroscopy. Next subsection (p. 31) illustrates the principle on a set of experimental Raman data and simulated Brillouin data, and showcases the performance of multi-excitation Brillouin spectroscopy on a challenging practical application.

Multi-excitation Raman spectroscopy utilizes the fact that a small shift in excitation wavelength does not affect the fluorescence emission spectrum (Kasha's rule), while the Raman peaks undergo a shift equal to the value of the incident wavelength shift. By acquiring four or more spectra from the same sample location with different excitation wavelengths, it is possible to computationally separate the constant and shifted components of the spectra. Using iterative signal estimation, it is possible to reconstruct the "pure" fluorescence emission and Raman spectra.

A similar observation can be applied to Brillouin spectroscopy: absorption spectrum – similarly to fluorescence emission – is invariant to excitation wavelength, while Brillouin and elastic peaks shift with the change in excitation wavelength. The main constraint of the multi-excitation Brillouin spectroscopy technique is staying within the absorption peak or peaks of the absorber (iodine for wavelengths around 532 nm), if that is the main strategy to suppress elastic scattering, This constraint is met with the use of a

stable tunable laser source and careful selection of the excitation shift values so that the excitation wavelength always remains within one of the absorption bands of iodine, or another molecular filter.

The reconstructed signal S is defined as $S \equiv [S_A^T \quad S_B^T]$, where S_A^T and S_B^T are pure absorption and Brillouin contributions respectively, each a vector of length N, the total length of S is $2N$. The recorded signal R can then be related to the reconstructed signal S using an operator matrix H of size $KN \times 2N$, where K is the total number of acquired spectra, as $HS = R$. The operator matrix H consists of square submatrices H_A and H_{B_k} describing relative spectral positions of each absorption and Brillouin component respectively, each of size $N \times N$:

$$H = \begin{bmatrix} H_A & H_{B_1} \\ \vdots & \vdots \\ H_A & H_{B_K} \end{bmatrix}$$

Since absorption spectrum is excitation wavelength invariant, all submatrices H_A are constant and are represented by an identity matrix. The submatrices for Brillouin spectrum component H_{B_k}, on the other hand, are formed based on the value of the excitation wavelength shift. The first Brillouin spectrum component ($k = 1$) is set as a reference spectrum, and its submatrix is represented by an identity matrix. The elements of H_{B_k} for each other spectrum ($k > 1$) equal to one on the minor diagonal corresponding to the shift in excitation wavelength and zero otherwise. Knowing R and H, it is impossible to explicitly solve for S, but we can obtain the separated components from

estimated reconstructed signal $\hat{S}$ using iterative algorithm, such as Lucy-Richardson algorithm:

$$\hat{x}_{i+1} = \hat{S}_i \times \left(H^T \left(R \div \left(H\hat{S}_i \right) \right) \right)$$

$$\hat{S}_{i+1} = \hat{x}_{i+1}$$

where $\times$ and $\div$ are element-wise multiplication and division respectively, and i is the iteration number. The initial estimate $\hat{S}_0 = \left[\hat{S}_{0A} \quad \hat{S}_{0B} \right]$, is taken to be the minimum and standard deviation over all K recorded spectra for absorption and Brillouin components respectively. Other strategies for selecting the initial estimate are suitable as well, the selected initial value only affects the number of iterations needed for reconstruction, not the result itself.

3.3 Examples

3.3.1. Validating the concept for Raman spectra retrieval

Figure 3.3 illustrates the results of component reconstruction on an example of multi-excitation Raman spectroscopy. Four Raman spectra of DMSO with addition of fluorescent dye were acquired, SNV-normalized and moving-average filtered prior to signal component estimation. The results of the reconstruction are shown after 100 iterations, with overlay displaying measurements from separate pure samples for comparison. It is clearly seen that the reconstruction of the signal from ME Raman spectra are very close to the measurements of the pure components, DMSO and fluorescent dye.

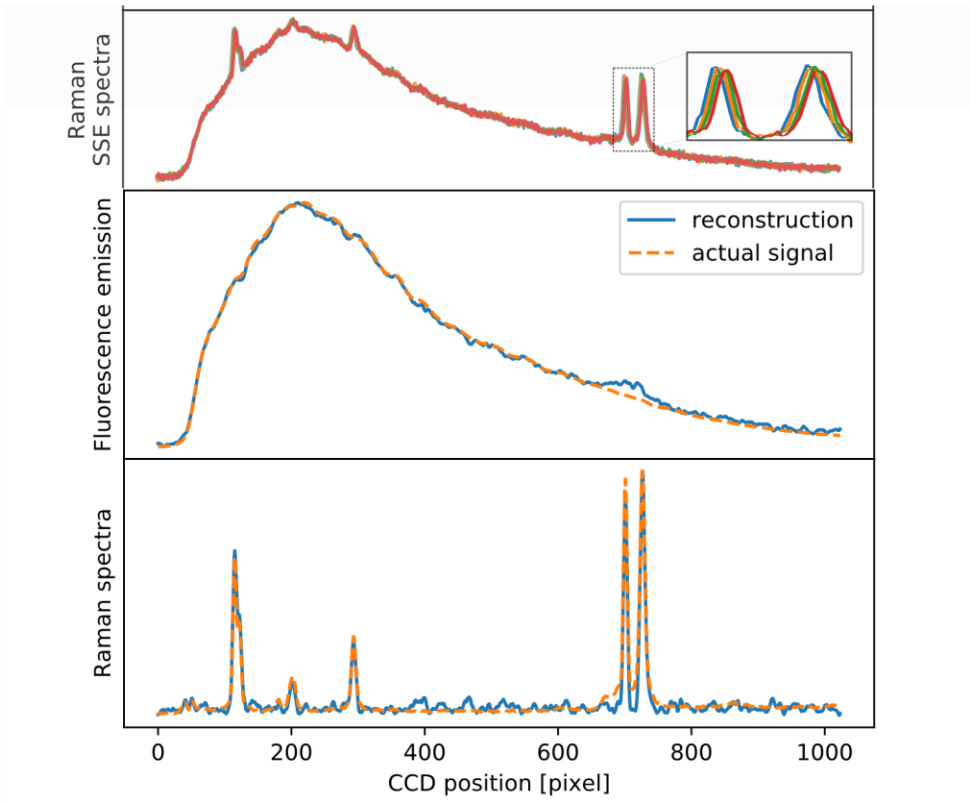

Figure 3.3 Example of ME Raman spectroscopy on DMSO and fluorescent dye solution sample: SNV-normalized ME spectra (top), signal reconstruction after 100 iterations (solid line) of fluorescence emission component (middle) and DMSO Raman spectrum component (bottom). An overlay of measurements acquired from pure separate samples are provided as overlaying dashed-line plots for comparison with the associated signal reconstruction.

3.3.2. Validating the concept for simulated Brillouin spectra

A set of simulated spectrally-shifted data is first used to illustrate the concept of multi-excitation Brillouin spectroscopy and Brillouin signal reconstruction. To produce the simulated spectra, a high-SNR Brillouin spectrum of water was shifted by approximately 0.15 GHz (2 pixels) per spectrum, and Gaussian random noise and constant iodine absorption spectrum were added to it (Figure 3.4, top). The signal reconstruction

was performed as outlined in the Subsection 3.2, and the resulting recovered Brillouin spectrum is provided after 100 iterations (Figure 3.4, bottom). It is readily apparent that the baseline distortion due to absorption is removed and the shapes of all peaks are consistent, allowing for a more accurate fit to a Lorentzian function.

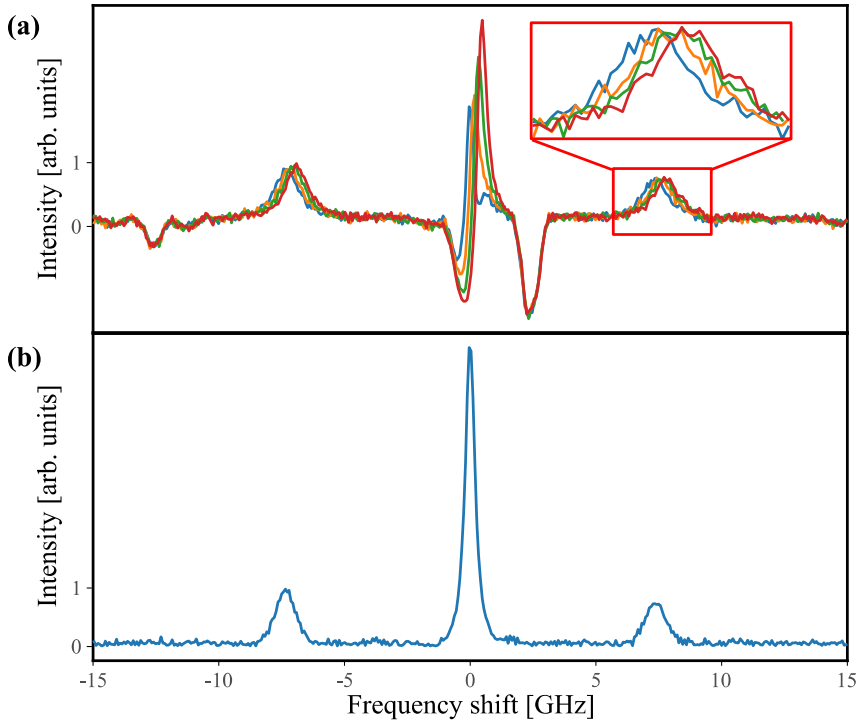

Figure 3.4 Example of multi-excitation Brillouin spectroscopy on simulated signal: Four spectrally-shifted simulated spectra with absorption-induced distortion of the baseline (top) and recovered Brillouin signal after 100 iterations (bottom).

3.3.3. Experimental validation of the multi-excitation Brillouin spectroscopy

Next, to illustrate the capabilities of the multi-excitation Brillouin spectroscopy in reconstructing Brillouin peaks from heavily distorted spectra (confocal pinhole removed), signal from a cream, a strong scatter was acquired with the iodine-filled cuvette heated to

80°C, resulting in excessive baseline distortion due to absorption. The Brillouin spectra were acquired using four excitation wavelengths, achieved using a tunable 1064 nm laser and a MgO:PPLN crystal; the final offsets from 532 nm were -70.65, -70.8, -70.95 and -71.1 pm, as defined for the seed diode laser. The top graph in Figure 3.5 shows the recorded spectra that would normally contain a triplet of peaks: Stokes and anti-Stokes Brillouin peaks and a single elastic peak. However, the level of noise and baseline distortion are so severe that the original four spectra cannot be used for analysis as it is unclear which features represent the Brillouin peaks. Using the method described in Subsection 3.2, it is possible to reconstruct the Brillouin signal; the reconstructed spectrum following 100 iterations is displayed the bottom graph in Figure 3.5. The recovered signal has clearly distinguishable Brillouin peaks surrounding the elastic peak and can be used in the routine Lorentzian fitting to calculate the value of Brillouin shift.

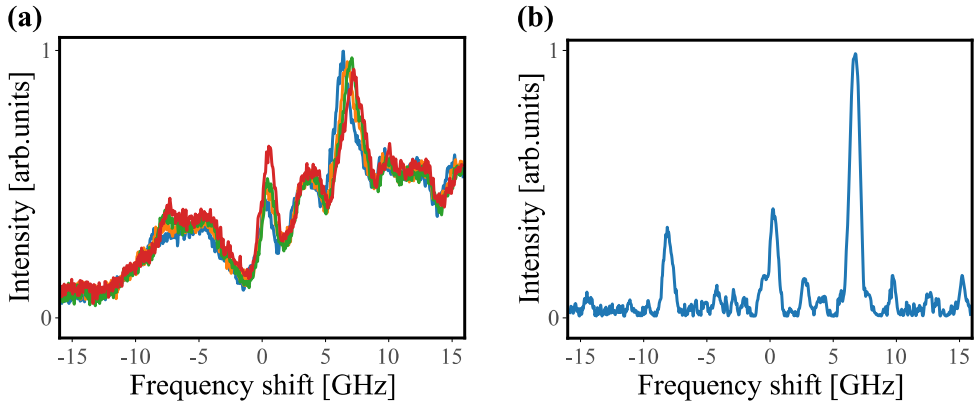

Figure 3.5 Example of multi-excitation Brillouin spectroscopy on cream sample: a) four SNV-normalized recorded spectra with excitation wavelength offset of -70.65, -70.8, -70.95 and -71.1 pm from 532 nm, and b) Brillouin signal reconstruction following 100 iterations.

3.4 Effect of multi-excitation Brillouin spectroscopy approach on SNR

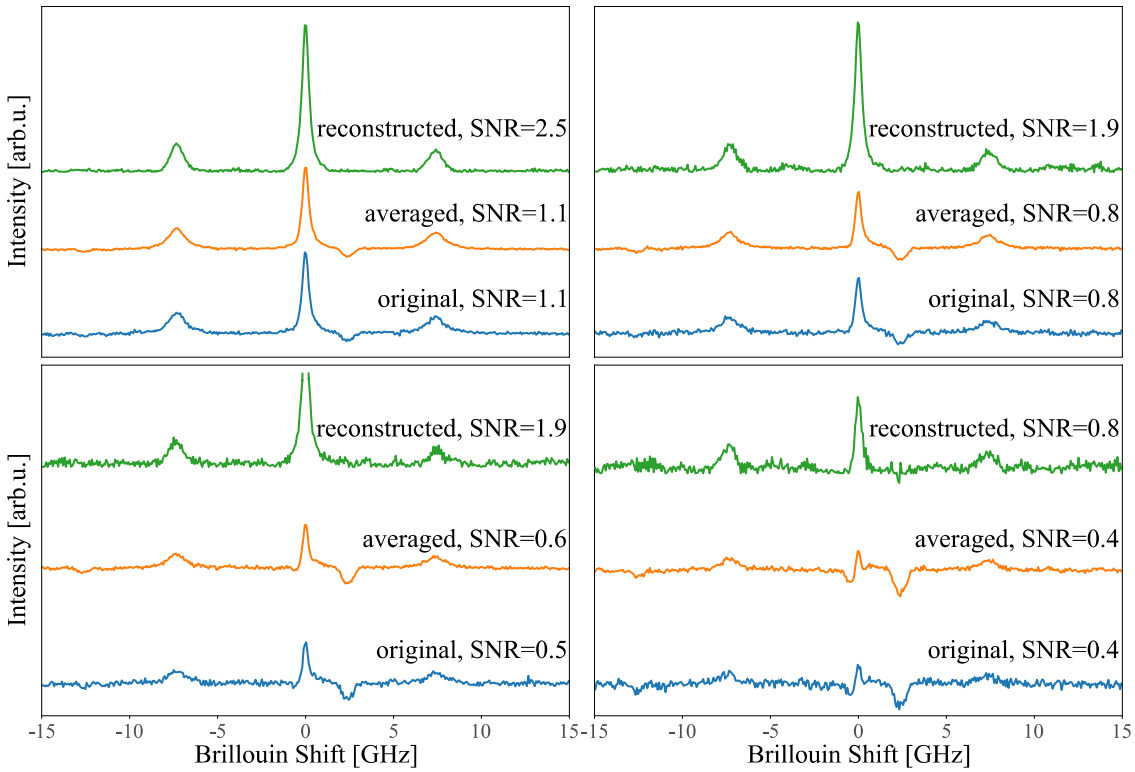

Figure 3.6 Simulated Brillouin spectra of variable signal strength with random noise and strong absorption: comparison of SNR of the original, averaged and reconstructed signals. Reconstructed method provides significant improvement over the original SNR, outperforming the averaged method, removing the distortion of the baseline and recovering the shape of the Brillouin peak.

Sub-section 3.3.3 illustrated the use of multi-excitation Brillouin spectroscopy on an extremely distorted sample to showcase the method's capability for Brillouin spectrum reconstruction. Realistically, most samples are unlikely to have distortions on such a severe level, however, multi-excitation approach provides an additional benefit of improving the spectrum's signal-to-noise ratio (SNR). Figure 3.6 displays four cases with simulated distorted signals with different levels of random noise, with SNR ranging from

1.1 to 0.4. In each case, an original spectrum is compared to the results from simple averaging of four non-shifted spectra and reconstruction from four excitation-shifted spectra. In each case, the multi-excitation reconstructed spectrum has greater SNR than the averaged equivalent.

3.5 Conclusions

In conclusion, using molecular filter for suppression of elastically scattered light can cause distortions of the Brillouin spectra of highly-scattering samples. Another potential source contributing to signal background are fluorescence emission from simultaneous fluorescence imaging or undesired ambient light reaching the detector. A distortion of the baseline or a partial absorption of Brillouin peak make it difficult to accurately determine the Brillouin shift. We present a novel approach for reconstruction of the Brillouin spectrum distorted by strong absorption or other constant contaminant – multi-excitation Brillouin spectroscopy. Multi-excitation Brillouin spectroscopy is a generalization of our previously reported Sequentially-Shifted Excitation (SSE) approach [61] that is not limited to a constant shift in excitation wavelength, but is suitable for any desired change in the excitation wavelength.

Multi-excitation Brillouin spectroscopy involves acquiring multiple Brillouin spectra using slightly offset excitation wavelengths and computationally reconstructing the pure Brillouin signal component. We first illustrate the concept by reconstructing the Brillouin signal from four simulated Brillouin spectra of water with strong absorption. Next, we demonstrate a practical application of multi-excitation Brillouin spectroscopy technique on recorded spectra of cream that are strongly distorted by excessive iodine

absorption. In the described work, we have used a tunable 1064 nm laser and a SHG crystal, which provided stable consistent shift in the excitation wavelength, but resulted in a variable power incident on the sample. In the future work we propose to use an acousto-optical modulator (AOM) to maintain constant power at the sample and improve the speed of excitation wavelength switching. Multi-excitation Brillouin spectroscopy is a powerful new tool that allows work with highly scattering samples or simultaneous acquisition of fluorescence imaging and greatly improves the quality of the final spectrum.

4. BIOMEDICAL APPLICATIONS OF BRILLOUIN SPECTROSCOPY*

A number of diseases and medical disorders result in a change in mechanical properties of the affected tissue. Among common examples of such conditions are osteoporosis, presbyopia and breast cancer. Brillouin spectroscopy is a powerful tool that can be utilized to investigate the differences in mechanical properties of healthy and diseased tissues and cells. Section 1, INTRODUCTION, contains an overview of Brillouin spectroscopy's capabilities. In the present section, I provide a selection of my research work that illustrates the usefulness of Brillouin elastography for investigation of diseases in animal models. The chosen examples are obesity in a rat model, cutaneous melanoma in a swine model and muscular dystrophy in a *Drosophila* larva model.

4.1 Obesity

4.1.1. Introduction

The prevalence of obesity has been on the rise over the past several decades; an estimated 1.9 billion adults worldwide were overweight or obese in 2014. [65] It is becoming a global epidemic, and the incidence of obesity and overweight is only expected to increase further. The causes of obesity range from poor dietary choices and lack of exercise to hereditary predisposition and adverse effects of medications. Obesity and overweight are associated with an increased risk of chronic health conditions, such as

---

* Part of this section is adapted with permission from "Optical assessment of changes in mechanical and chemical properties of adipose tissue in diet-induced obese rats," by M. Troyanova-Wood, *et al.*, J. Biophotonics **10**, 1694–1702 (2017) (Reference [43]) and from "Differentiating melanoma and healthy tissues based on elasticity-specific Brillouin microspectroscopy," by M. Troyanova-Wood, *et al.*, Biomed. Opt. Express **10**, 1774–1781 (2019) (Reference [59]).

coronary heart disease, hypertension, diabetes, sleep-breathing disorders and some types of cancer. [66,67]

Obesity and overweight are characterized by increased adiposity – the ratio of the lipids stored in adipose tissue to the total body mass. The increase in lipid storage is accomplished with both an enlargement of the existing adipocytes (hypertrophy), and an increase in the number of new adipocytes (hyperplasia). During the progression of obesity the adipose tissue undergoes remodeling, which includes the changes in the cell type and distribution, size and function, as well as changes to the composition and structure of the extracellular matrix (ECM). [68,69]

The changes occurring during weight gain have an effect on the mechanical properties of both adipocytes and the adipose tissue (AT). On microscopic level, the mechanical properties of adipocytes are largely determined by the number, size, and content of their lipid droplets. [70] On the macroscopic level the stiffness of the AT is determined by the ECM and cellular composition of the tissue (including type, size and distribution of cells). [68,71] Adipocytes are mechanosensitive and mechanoresponsive cells whose differentiation and function are affected by the applied stress and mechanical properties of their environment, [72,73] which is, in turn, affected by the surrounding adipocytes.

The mechanical properties of AT are important to its proper function. Changes in these properties may interfere with the role of the tissue in protection against mechanical stress, while the changes in the adipocytes' environment have a potential to affect lipid storage. However, there is limited information on mechanical properties of AT. [74] The

studies that did investigate the elastic properties of AT used destructive tension and compression testing and investigated only bulk properties of the sampled tissue. These techniques cannot be applied to investigation of elastic properties of individual adipocytes, which requires greater spatial resolution. On the other hand, atomic force microscopy, [70] while suitable for measurements of individual cells, cannot investigate tissue mechanical properties. There is, therefore, a need for a method of mechanical characterization of AT that is suitable for noninvasive analysis of both bulk tissue and individual cells.

Unlike other techniques, elastography based on Brillouin scattering provides non-destructive measurements of elasticity (specifically, the high-frequency longitudinal elastic modulus) with high spatial resolution. Brillouin scattering is an inelastic scattering phenomenon that occurs due to the interaction of the incident photons with the sample's spontaneous phonons. The inelastic interaction results in a small, 1-10 GHz, frequency shift of the scattered photon compared to that of the incident light. This frequency shift, which is often called Brillouin shift, follows $\Delta\nu_B = \pm 2\,\frac{n\,V_s}{\lambda_0}\,\sin(\frac{\theta}{2})$, where n is the material's index of refraction, V_s is the speed of sound in the material, λ_0 is the wavelength of the incident light, and θ is the angle between the incident and scattered light (the collection angle).

The measured Brillouin shift can be used to assess material's mechanical properties, such as speed of sound and, correspondingly, the high-frequency longitudinal elastic modulus. The speed of sound for collection angle $\theta = \pi$ can be calculated from the measured Brillouin frequency shift: $V_s = \frac{\Delta\nu_B\,\lambda_0}{2\,n}$. The speed of sound is related to the real

part of the longitudinal modulus, $M', as\ V_s = \sqrt{\frac{M'}{\rho}}$, where ρ is the material's mass density. The high-frequency longitudinal elastic modulus can, therefore, be calculated directly from the Brillouin shift for backscattered signal collection as $M' = \frac{1}{4}\ \rho\ (\frac{\Delta\nu_B\ \lambda_0}{n})^2$. Brillouin elastography (also known as Brillouin spectroscopy), an emerging spectroscopic technique, [52,75] is capable of assessing the elasticity for biomedical applications on the level of tissue [32,33,76] and individual cells. [36,37]

The obesity-related changes in the AT mechanical properties are related to the composition and organization of ECM; [71] however the accumulation of the collagen is not the only contribution to the increase in stiffness. [77] Evaluating the changes in the composition of AT would prove a useful tool to understand the changes in the elasticity. There are many different approaches to chemical assessment of the AT, such as fluorescence imaging, second-harmonic generation microscopy, [71] and Raman spectroscopy. [78,79] Raman spectroscopy can be combined with Brillouin elastography for simultaneous measurements. [37,42,80,81] Raman spectroscopy is based on inelastic scattering that occurs due to specific molecular vibrations in the molecule of interest. The scattered photon exhibits a frequency shift compared to the frequency of the incident photon. The full Raman spectrum will, thus, represent the ensemble of vibrations of the molecule under study and can be used to chemically characterize the sample. The Brillouin and Raman spectral measurements can be recorded simultaneously from the same position on the sample to provide complimentary assessment of the sample's mechanical properties and chemical composition. [37,42]

The AT is characterized into two distinct forms: white adipose tissue (WAT) and brown adipose tissue (BAT). The two types of AT possess different structural characteristics, biological functions, and localization. [82] The mechanical properties and structure of the AT are generally determined by the mechanical load acted upon it, and vary by the anatomical location. [74] White and brown adipose are associated differently with obesity, and may exhibit varying degree of changes. The current study obtains measurements of elasticity and composition from both white and brown adipose in lean and obese rodents.

Mechanical properties of AT are crucial for its proper function, and they can be affected by obesity and overweight on both microscopic and macroscopic levels. However, there are few studies that focused on evaluating the obesity-induced changes in AT's elastic properties, most of which used destructive techniques that assessed the properties in either tissue or cell culture, but are not suitable for both. Additionally, these studies either did not obtain chemical information, or obtained chemical information separately from the mechanical measurements. In the present study, we have utilized non-destructive Brillouin and Raman spectroscopy to obtain simultaneous mechanical and chemical information, allowing for a more thorough characterization of the sampled location. We have successfully assessed the changes in mechanical properties and chemical composition of BAT and WAT in lean (control group) and diet-induced obese (high-fat diet, HFD, group) rats. The results support our hypothesis that the stiffness and lipid content of adipose tissues increases in obesity, with an additional indication that the BAT is affected greater than the WAT.

4.1.2. Materials and methods

4.1.2.1. Animals

The tissue samples for the current study were obtained from adult male Sprague-Dawley rats of the same age, 7-months old. All animal procedures were reviewed and approved by our Institutional Animal Care and Use Committee and were in accordance with federal and local regulations. The rats were divided into two groups, 3 per group, and were given unlimited access to food and water. The diet-induced obese group received high-fat diet (HFD) with 60% energy from fat (#58Y1, TestDiet, St. Louis, MO, USA), while the control group received matched regular diet with 10% energy from fat (#58Y2, TestDiet, St. Louis, MO, USA). The animals were sacrificed after 16 weeks. On the experimental day, all rats were anesthetized with a solution containing a combination of Fentanyl/Droperidol (0.3 mL/kg IM) and Diazepam (2.5 mg/kg IM). Prior to sample collection, the rat was shaved in the areas of interest to prevent hair getting on the samples. Subsequently, the chest was opened (which is a terminal procedure) and the samples of white and brown adipose tissues were collected immediately post mortem through surgical extraction.

4.1.2.2. Sample preparation and analysis

WAT was collected from inguinal adipose deposit. The euthanized rat was placed on its back, the skin on lower abdomen was lifted using tweezers, and incised, revealing a large white fat deposit located between the abdomen and the hind limb. The sample of the WAT was dissected and placed in a sealed container on ice.

Next, BAT was obtained from the interscapular brown adipose tissue (IBAT) deposit. The animal was placed on the abdomen, and the skin approximately one inch below the shoulder blades was grasped with tweezers, lifted, and incised. The skin was widely cut laterally and forward to open the shoulder region. The revealed lightly-colored fat pad contained IBAT covered with a thin layer of white adipose. The WAT was carefully lifted and excised, revealing a butterfly-shaped darker-colored BAT. The brown fat pad was carefully dissected to ensure no white adipose or muscle remained attached to the sample, and placed in a sealed container on ice.

Both the Raman and Brillouin spectral data were simultaneously collected from the same location on the same day of tissue extraction. The AT samples were brought to room temperature prior to data acquisition.

4.1.2.3. Experimental setup

The schematic for the Raman/Brillouin spectrometer is shown in Figure 4.1, a; the detailed description of the spectrometer is discussed in Reference [83]. Raman and Brillouin spectra were collected simultaneously using a 532 nm single-frequency laser as the source of incident radiation (Lasermate Group Inc.; model: GMSL-532-100FHA; nominal linewidth ~640 kHz, power output ~120 mW), delivering ~30 mW of power onto the sample. A half-wave-plate was placed before a polarizing beamsplitter to adjust the power of light incident onto the sample. The polarizing beamsplitter redirected the incident light towards the infinity-corrected 20x microscope objective lens (Nikon Inc., CFI Plan Fluor 20x, N.A. = 0.5), providing a beam spot diameter of ~1.3 μm on the sample.

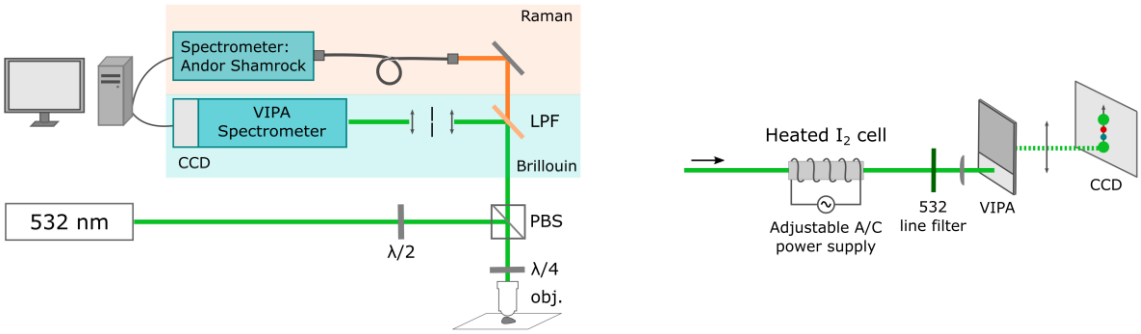

Figure 4.1 (a) Schematic diagram of instrumental setup for simultaneous Raman and Brillouin spectroscopy, and (b) detailed diagram of the Brillouin spectrometer.

The microscope objective lens was used to focus the incident light onto the sample and to collect the backscattered signal. The finite NA objective lenses contribute to a spectral broadening of the Brillouin peaks, which is more pronounced when using high NA objectives (NA>0.5). A lower NA objective limits this spectral broadening at a sacrifice of the spatial resolution. The NA=0.5 objective lens used in the present study causes insignificant broadening due to the 180° signal collection angle. The backscattering geometry results in a less pronounced spectral broadening, compared to a 90° collection angle. [28] Additionally, due to backscattered collection geometry, measurements of Brillouin scattering contain mainly contribution from longitudinal wave, and not the shear (transverse) waves. [29]

A quarter-wave-plate was placed before the objective to rotate the polarization of the backscattered beam by 90° in order to direct it towards the Brillouin and Raman spectrometers. The backscattered beam was split by a long-pass filter; the longer wavelengths were passed through towards the home-built Raman spectrometer (fiber-coupled Shamrock 303i spectrometer with the attached iDUS 401 CCD, Andor, Inc.;

spectral resolution of approximately 3.5 cm^{-1}, or 0.1 nm), while the rest of the collected light was redirected towards the Brillouin spectrometer (Figure 4.1, b).

The Brillouin spectrometer (Figure 4.1, b) utilized a temperature-tunable iodine absorption cell (Opthos Instruments, Inc.) set to 112°C as an ultra-narrow notch filter that absorbed the undesired elastic scattered light. The shape of Brillouin spectra is often affected by the absorption of the iodine cell; [50] however, the absorption spectrum of molecular iodine is well characterized (see, for example, Reference [47]), and the spectral amendments can be taken into account for a very precise (±1 MHz, or ~3.3E-5 cm^{-1}) Brillouin spectral shift identification. [84] A 532-nm line filter was placed after the cell to block the undesired fluorescence from the iodine. The filter was followed by the virtually imaged phase array (VIPA; model: OP-5642, Light Machinery Inc.) spectrometer design as described by Scarcelli and Yun. [85]

4.1.2.4. Data processing and analysis

Spectral data were analyzed using OriginPro 2016, Sr1 (OriginLab, Northampton, MA); the results were expressed as mean ± SEM (average n=15 in each subgroup).

To process the Raman measurements 5 replicate spectra (1 second acquisition time) from each spatial location were averaged after dark background subtraction. The spectra were smoothed using a moving average method (5 points window), baseline corrected, and vector normalized to facilitate comparison.

To process the Brillouin spectra, 5 replicate spectra (1 second acquisition time) from each spatial location were averaged, and the Lorentzian function fit was used to determine the central frequency of Brillouin peaks and residual elastic peaks. The spectral

position on the CCD was converted to GHz using third order polynomial interpolation and the fact that the spacing between the elastic peaks is equal to the free spectral range (FSR) of the VIPA, 33.334 GHz. The value of the Brillouin shift was determined as difference between frequencies of the elastic and Anti-Stokes Brillouin peaks.

The measurements from control and HFD groups were compared using one-way analysis of variance (ANOVA) to determine if there are statistically significant differences between the groups. The data that showed great distribution, the control BAT and WAT, were also grouped into clusters based on their similarity using K-means clustering analysis (KCA). The KCA is a simple unsupervised learning algorithm that groups a dataset into a user-predefined number of clusters based on their spectral similarity. The KCA was repeated several times for an increasing number of user-specified clusters, until the spectra of two or more clusters could not be easily distinguished from each other.

4.1.3. Results and discussion

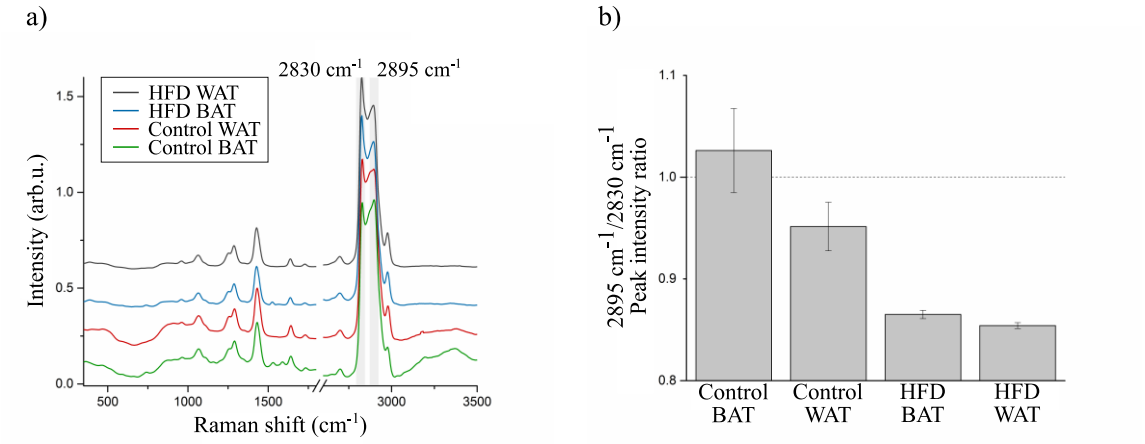

Figure 4.2 (a) Mean Raman spectra and (b) protein-to-lipid ratio (ratio of peaks' intensities at 2895 and 2830 cm^{-1}) of control and high-fat-diet (HFD) groups' brown (BAT) and white (WAT) adipose tissues.

The averaged Raman spectra brown and white adipose tissues in each group are shown in Figure 4.2, a; the plots are offset for clarity. The Raman spectra of AT of both groups are dominated by high-intensity bands in the 2500-3000 cm^{-1} region, associated with CH, CH_2, and CH_3 symmetric and asymmetric stretching in lipids and proteins. [86] Lipids are the main contributor to the lower energy level peak, while the higher energy peak represents the vibrations present in adipose's protein. [79]

While there are some minor changes in the spectra between control and HFD groups, the most pronounced of them occur in the abovementioned region. The two peaks in the region, located at 2895 and 2830 cm^{-1} (highlighted in gray), were used to estimate the protein-to-lipid ratio in the sampled area by calculating the ratio of the peaks' intensities. The results are displayed in Figure 4.2, b, as mean ± SEM.

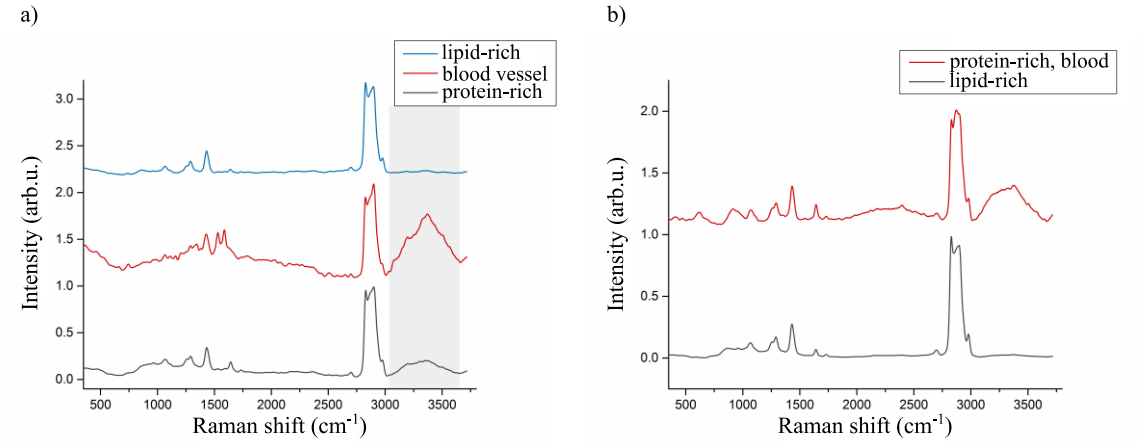

Figure 4.3 Mean Raman spectra calculated for different clusters obtained after KCA (K-means clustering analysis) on the control (a) brown (BAT) and (b) white (WAT) adipose tissue.

The BAT of the control group displayed, on average, a greater relative amount of protein than any other subgroup. The high protein content of BAT in the control group is expected due to its composition and function. [82] Overall, the Raman spectra of control BAT and WAT have displayed greater diversity of composition than the AT of the HFD group. Using KCA, the measurements of control BAT can be broadly divided into 3 groups (Figure 4.3, a) based on their Raman spectra: 1) lipid-rich and 2) protein-rich areas, and 3) blood vessel (high water content, region highlighted in gray). The WAT of the control group can be divided into only 2 groups (Figure 4.3, b): 1) lipid-rich, and 2) protein-rich with high water content (blood vessel).

The results indicate that the consumption of a high-fat diet has a greater effect on the BAT than on the WAT. The changes in the protein-to-lipid ratio of both the BAT and WAT are statistically significant ($p \leq 0.01$) between the control and HFD groups.

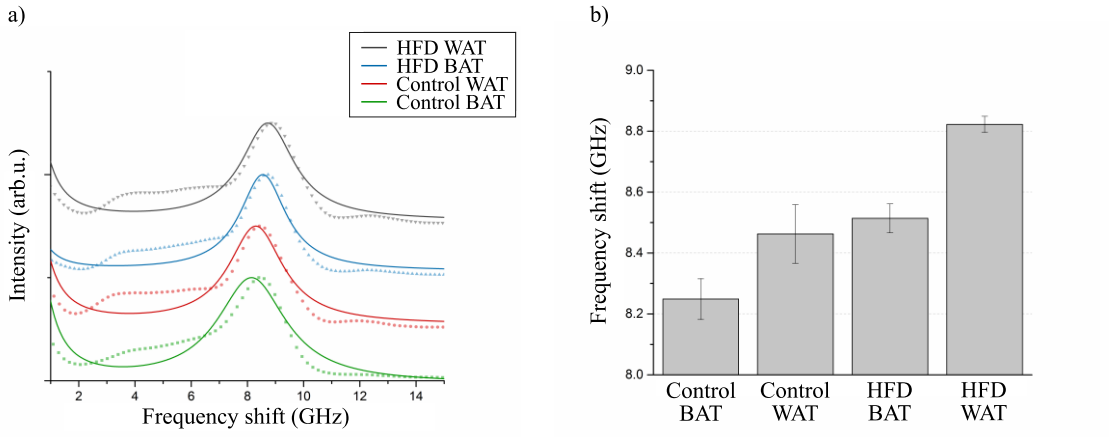

Figure 4.4 (a) Mean fitted Brillouin peaks and (b) Brillouin shifts of control and high-fat-diet (HFD) groups' brown (BAT) and white (WAT) adipose tissue.

Figure 4.4, a displays Lorentzian function-fitted averaged Anti-Stokes Brillouin peaks of BAT and WAT in control and HFD groups. For clarity, the spectra are vertically offset and the individual data points are not displayed. The central frequencies of the Brillouin peaks were determined from the fit, and are summarized in Figure 4.4, b; the data are shown as mean ± SEM.

A greater Brillouin shift value corresponds to stiffer tissue. Overall, the control BAT is the softest tissue out of the measured samples, while the WAT of the HFD group has the greatest Brillouin shift. The stiffness of AT increases between the control group and the HFD group; Brillouin shifts of control group's BAT and WAT are statistically significantly different ($p \leq 0.01$) from those of the HFD group.

As discussed in the Introduction section, longitudinal high-frequency elastic modulus M' can be calculated from the value of the Brillouin shift as $M' = \frac{1}{4}\,\rho\,(\frac{\Delta\nu_B\,\lambda_0}{n})^2$ (for backscattered collection geometry). Additionally, the speed of sound in the material can be determined as $V_s = \frac{\Delta\nu_B\,\lambda_0}{2\,n}$. In both abovementioned equations, $\Delta\nu_B$ is the Brillouin shift, n is the material's index of refraction, λ_0 is the wavelength of the incident light, and ρ is the material's mass density. While a literature search failed to yield values of density and refractive index of WAT and BAT specifically, we were able to estimate the elastic modulus and speed of sound using general values of adipose refractive index, $n = 1.455$, [87] and density, $\rho = 0.916$. [88] The values of Brillouin shift, longitudinal high-frequency elastic modulus, and speed of sound are summarized in Table 4.1. Traditionally, the Brillouin shift is expressed in GHz, but converted values in cm^{-1} units are added to the table for comparison purposes.

Table 4.1 Measured values of Brillouin shift, and calculated elastic moduli and speed of sound of brown (BAT) and white (WAT) adipose tissue in control and diet-induced obese (HFD: high-fat diet) groups. All values are presented as mean ± SEM.

Tissue	Brillouin shift [GHz]	Brillouin shift [cm^{-1}]	Elastic modulus [GPa]	Speed of sound [m/s]
Control BAT	8.249 ± 0.067	0.275 ± 0.002	2.083 ± 1.39E-4	1508 ± 12
Control WAT	8.463 ± 0.096	0.282 ± 0.003	2.193 ± 2.84E-04	1547 ± 18
HFD BAT	8.514 ± 0.047	0.284 ± 0.001	2.219 ± 6.91E-05	1556 ± 9
HFD WAT	8.822 ± 0.027	0.294 ± 0.001	2.383 ± 2.16E-05	1613 ± 5

The control group's BAT and WAT have a greater variation of stiffness than the adipose of the HFD group. The simultaneously obtained Raman spectra also showed greater distribution in these two groups; however, separating the Brillouin shifts into the clusters based on their Raman spectra did not yield smaller distribution of Brillouin shifts. Instead, KCA of the control group's Brillouin measurements resulted in three clusters that matched the animal the tissue was harvested from. Additionally, for each animal, the WAT displayed a greater Brillouin shift than the BAT ($p \leq 0.05$), indicating the white adipose is generally stiffer.

Studies show that obesity is accompanied with AT fibrosis, characterized by collagen fiber accumulation, which is correlated with increased AT stiffness in obese individuals (see, for example, Reference [77]). If the amount of collagen increased at the same rate as the accumulation of lipids due to adipocyte hypertrophy or hyperplasia, the Raman spectra would show little change in the protein-lipid ratio.

However, in our measurements we see a significant drop in the protein content relative to the amount of lipids, suggesting that the accumulation of lipids outpaces the

increase in collagen. The observed increase in the stiffness of both BAT and WAT between control and HFD groups is then most likely the result of adipocyte enlargement and greater crosslinking of collagen fibers, both of which are present in obesity and correlated to an increase in stiffness. [70,72]

4.1.4. Conclusion

In the present study we, for the first time, have evaluated the effect of high-fat diet (HFD) on elasticity and chemical composition of brown (BAT) and white (WAT) adipose tissues using concurrent spectroscopic techniques. The novel simultaneous chemical and mechanical assessment of the adipose tissue (AT) was achieved using Raman and Brillouin spectroscopies. Overall, the stiffness of both BAT and WAT is significantly greater in HFD group compared to the control, as indicated by an increase in their Brillouin shift, and, therefore, their elastic moduli. Additionally, while the stiffness of AT of the control group varied slightly from animal to animal, the BAT generally possessed a lower Brillouin shift than the WAT. Elasticity measurements in studies of obesity's effect on adipose [74,77] and lipid accumulation's effect on adipocytes [70] indirectly support our findings. The Raman spectra were used to estimate the protein to lipid ratio in the sampled location, and the results indicate that the amount of lipids increases greatly in the HFD group, as the ratio decreases. The Raman spectra also indicate that control BAT possesses a greater structural and chemical diversity, while both AT of the HFD group are more homogeneous. The HFD-induced changes are more profound in the brown adipose.

We have shown, using Brillouin elastography, that elasticity of interscapular BAT and inguinal WAT is affected by an HFD, with the stiffness of the tissues increasing.

However, expanding the study to include other fat depots would provide a better understanding on the obesity's effect on different AT locations. Several studies have shown that different AT depots possess different elastic modulus, [71,74] and ECM composition and structure. [89,90] The degree of obesity-associated inflammation, [91] and the macrophage accumulation [92] are also location-dependent. Additionally, progression of obesity differs between male and female rodents, [93] so the HFD-induced elasticity changes are likely different between the two groups. We believe that our experimental approach validated in this study opens wide possibilities to obtain wide spectrum of this necessary scientific knowledge.

We note that while, at present, it takes about 1 second to collect the data from a single point, coherent optical spectroscopies based on coherent anti-Stokes Raman scattering and stimulated Raman scattering, [94,95] and coherent and impulsive Brillouin scattering [96,97] have a capability of tremendously speeding up the current data acquisition process, while providing microscopic spatial resolution in a depth of a tissue. [98] By maintaining the peak power of laser beams below the safety limits, [99,100] such as in the present study, *in vivo* measurements become feasible, providing an opportunity to implement our experimental approach in future clinical studies.

4.2 Melanoma

4.2.1. Introduction

The ability of melanoma to spread throughout the body by reaching lymph or blood vessels makes it the deadliest of skin cancers [101]. While not as common as other

cutaneous cancers, the incidence of malignant melanoma is on the rise, having increased by three times between 1970s and 2000s in the U.S. [102], resulting in an estimated 9,940 fatalities within the last year [103]. Melanoma that is detected early can be successfully treated; however, with the progression of the disease, the mortality rate rapidly increases, reaching 94% in the distant stage [103]. The survival rate, therefore, greatly depends upon early diagnosis of the melanoma.

The location of the melanoma on the surface of the skin makes it visible and accessible, however, the diagnosis of this cancer is not simple. The appearance of malignant melanoma is similar to other pigmented skin lesions, both benign and malignant. Morphological features form the basis of most approaches to clinical diagnosis of melanoma. If initial evaluation suggests a possibility of melanoma, the biopsy of the lesion is taken for a histological verification of the diagnosis, which may take several days. The common diagnostic algorithm is evaluation of the lesion's asymmetry, border irregularity, color and diameter (ABCD). Most often the evaluation is achieved by naked-eye examination, the sensitivity of which is 85% [104]. Dermoscopy, or dermatoscopy, a technique with greater sensitivity and specificity of the diagnosis, utilizes a microscopic evaluation of the lesion's morphological features [105,106].

However, evaluation of morphological features is not the only method to diagnose malignant melanoma. A lot of research is conducted on methods that aim to increase the accuracy of melanoma diagnosis and aid pre-operative assessment of tumor margins and thickness. Among them are conventional and high-frequency ultrasound [12,107–109],

ultrasound elastography [12,109,110], multispectral imaging [111–113], MRI [114,115], and Raman spectroscopy [116–118].

Of particular interest is the diagnosis based on the change in the mechanical properties between malignant and healthy tissue or cells. The rigidity of many tumor types compared to the surrounding normal tissue is well known and is routinely used; a common example is palpation during breast cancer screening [119]. This variation in elasticity between the malignant mass and the normal tissue can be utilized to achieve a non-invasive diagnosis. One available elasticity-specific technique, ultrasound elastography [14], determines the elasticity score of the tissue by comparing measurements before and after applied compression. This method has been used to successfully discriminate between benign and malignant lesions in breast [10,11] and prostate [11], and it displayed potential in diagnosis of malignant melanoma [110]. However, ultrasound elastography measures the macroscopic elasticity, which often differs from the elasticity on a microscale [120–122]. For example, tumors are stiffer than healthy tissue on a macroscopic level, but individual cancerous cells of many cancer types are softer [123,124], which is related to their ability to invade and metastasize [26,27]. Interestingly, that is not always the case, and AFM elastography study on melanocytes has shown that pigmented human melanoma cells are stiffer than both healthy melanocytes and non-pigmented melanoma cells from same cell line [125]. Evaluating microelasticity instead of macroelasticity can be used to identify the tumor margin with high resolution, and can become a valuable tool for research of cancer progression. Brillouin spectroscopy

can be used to probe the elastic properties of bulk tissue, while also providing an adequate spatial resolution to measure elasticity of individual cells.

Brillouin microspectroscopy is an emerging technique for measuring the viscosity and elasticity of a sample. Brillouin spectroscopy is based on the inelastic interaction of the incident photons and investigated material's spontaneous acoustic phonons. The incident wave undergoes a small, 1-10 GHz, change in frequency– called the Brillouin shift, which is related to the material's high-frequency elastic modulus. The Brillouin shift is equal to $\triangle \nu_B = \pm 2 \frac{nV_s}{\lambda_0} \sin\left(\frac{\theta}{2}\right)$, where n and V_s are the refractive index and the speed of sound in the material, λ_0 is the wavelength of the incident light and θ is the collection angle. The above equation can be used to directly calculate the speed of sound from the Brillouin shift. Assuming the collection angle of $\theta = \pi$, such as in the present study, the speed of sound is then calculated as: $V_s = \frac{\triangle \nu_B \lambda_0}{2n}$. Furthermore, the real part of the longitudinal modulus M' is related to the speed of sound and the material's mass density, ρ, as $M' = {V_s}^2 \rho$. This relationship can be used to determine the longitudinal modulus from the Brillouin shift; for a signal collection limited to $\theta = \pi$ it is $M' = \frac{1}{4} \rho \left(\frac{\triangle \nu_B \lambda_0}{n}\right)^2$.

Brillouin spectroscopy is a non-destructive and label-free approach to determining viscoelasticity of a wide range of materials. Brillouin spectroscopy has been successfully applied in recent years in a number of biological applications [43,56,58,126–131]. Brillouin spectroscopy nondestructively measures elasticity with high spatial resolution, making it a feasible method to differentiate between healthy tissue and tumors.

The animal model for malignant melanoma used in this study is Sinclair miniature swine. Sinclair miniature swine is an accepted model of human melanoma, first used in a study of malignant melanocytic tumors in 1974 [132]. These animals possess melanoma lesions at birth, or develop them within a few days after birth. These malignant lesions are histopathologically similar to human malignant melanoma, albeit with greater melanin concentration. However, the melanoma in Sinclair swine spontaneously regress within weeks, and new lesions do not form. A loss of pigmentation commonly accompanies the melanoma regression in the area surrounding the lesion, and is frequently present elsewhere on the body. The preliminary results of Brillouin spectroscopy measurements of Sinclair swine melanoma have been published by our group previously [52,76]. In the present study we have obtained multiple measurements from both a normal non-regressing melanoma and a regressing melanoma with a visible depigmentation around the primary lesion. We hypothesize that the elasticity of the regressing tumor will be close or equal to the elasticity of the surrounding healthy tissue, while the non-regressing melanoma will be the stiffest of the three sample types. It is worth noting that change in the Brillouin shift can be attributed to both change in tissue elasticity and refractive index. Melanocytes in non-regressing melanoma have a greater number of melanin granules within the cell than those in the normal tissue. The higher concentration of melanin would reflect in a higher absorption and refractive index of the lesion. At the same time, the higher melanin content in melanoma melanocytes has been shown to result in higher cell stiffness, measured with AFM elastography [125]. While it is impossible to state by what extent the increase in the Brillouin shift can be attributed to a change in stiffness alone, the conclusion that

melanoma lesion is stiffer than surrounding normal tissue is supported by published literature, for example, the real-time tissue elastography study [110].

We hypothesize that Brillouin microspectroscopy can be used to distinguish malignant tumors from surrounding normal tissue. In this report, we demonstrate the application of this method on an animal model of malignant melanoma. We have successfully obtained Brillouin shift measurements from healthy, cancerous and regressing tissues and found the variations in the Brillouin shift between all three tissue types to be statistically significant.

4.2.2. Materials and methods

4.2.2.1. Melanoma samples

The samples of malignant melanoma, collected from Sinclair miniature swine, were kindly provided by Dr. D. Kraemer (College of Veterinary Medicine & Biomedical Sciences; Texas A&M University). All animal procedures were approved by our Institutional Animal Care and Use Committee and were in accordance with federal and local regulations. The melanomas with 2 cm margins were surgically removed from a 6-weeks old male Sinclair miniature swine under anesthesia. One of the lesions was identified as a non-regressing melanoma (Figure 4.5, a, circle marking the lesion), while the second tumor displayed depigmentation around the lesion, and was determined to be a regressing melanoma (Figure 4.5, b, circle marking the lesion and arrow pointing to the area of depigmentation). The samples were placed in sealed containers filled with phosphate saline buffer (PBS) on ice, and the Brillouin measurements were obtained on the same day.

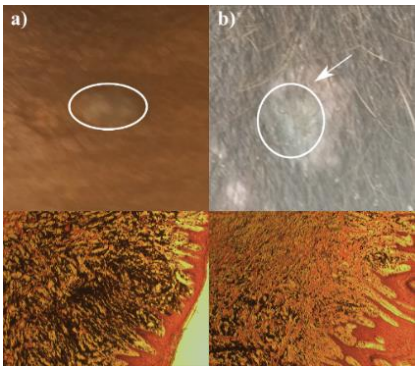

Figure 4.5 Photos (top, circles mark the lesions, arrow points to the area of depigmentation) and corresponding histology slides of lesion cross-section (bottom, H&E stain) of: (a) normal non-regressing melanoma and (b) regressing melanoma.

An average of 3 replicate Brillouin spectra from 8 different locations per tissue type were obtained from the central areas of the malignant growths and from the healthy tissue regions at a distance of 1 cm from the sample's edge. In the regressing melanoma sample, the healthy region was sampled away from the area of depigmentation. The integration time was 60 s and the incident power on the sample did not exceed 20 mW; no obvious damage to the sampled area was detected following the data collection.

4.2.2.2. Brillouin spectroscopy setup

Figure 4.6 shows the schematic diagram of the optical setup for Brillouin microspectroscopy, which followed our earlier design [50,83]. More detail on the system's latest design and performance is provided in Coker *et al*. [51].

A 532-nm single- frequency laser (Lasermate Inc.; GMSL-532-100FHA) served as the source of the incident light. The incident light passed through a polarizing beamsplitter towards the infinity-corrected microscope objective lens (Nikon Inc., CFI Plan Fluor 20x, N.A. = 0.5), which both focused the incident light onto the sample, and

collected the backscattered signal. A quarter-wave plate and the polarizing beamsplitter redirected the collected signal towards the VIPA spectrometer, with a pinhole placed before the spectrometer serving to reduce the amount of out-of-focus light reaching the detector. The VIPA spectrometer consisted of a temperature-tunable iodine absorption cell (Opthos Instruments, Inc.) set to 112°C which served as an ultra-narrow notch filter, and 532-nm line filter that filtered the undesired laser, Raman and I_2 fluorescence frequencies, followed by VIPA and the CCD.

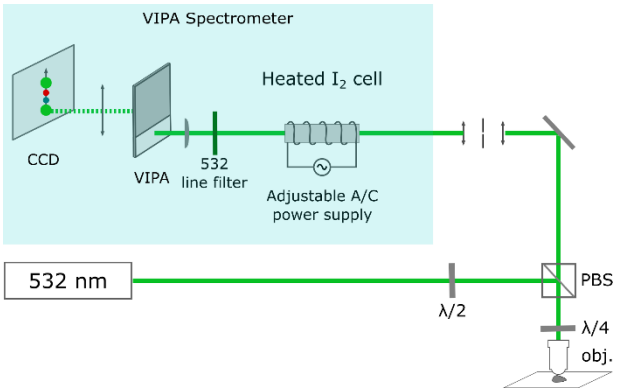

Figure 4.6 Schematic diagram of instrumental setup for Brillouin spectroscopy. The heated iodine cell served as an ultra-narrow notch filter. Abbreviations: PBS – polarizing beamsplitter, obj. – 20x objective lens (NA=0.5), λ/2 – half-wave plate and λ/4 – quarter-wave plate.

4.2.3. Results and discussion

To illustrate typical raw and processed Brillouin spectra, an example from a single measurement of non-regressing and regressing melanomas, and the healthy tissue region is presented in Figure 4.7, a. Notably, the SNR between the three spectra is different, even though the acquisition parameters remained unchanged. The healthy tissue possesses the greatest SNR, while the signal from the non-regressing melanoma has the smallest SNR.

These differences in the signal quality is likely due to the increased absorption of the incident light by the melanin, the concentration of which is the greatest in the non-regressing melanoma. The Brillouin peaks are fit with the Lorentzian function to obtain their central frequency, as shown in Figure 4.7, b. Both tumors and healthy tissue possess notably different Brillouin shifts; the results of all measurements (N=8 per tissue type) are displayed as mean ± standard deviation in Figure 4.8.

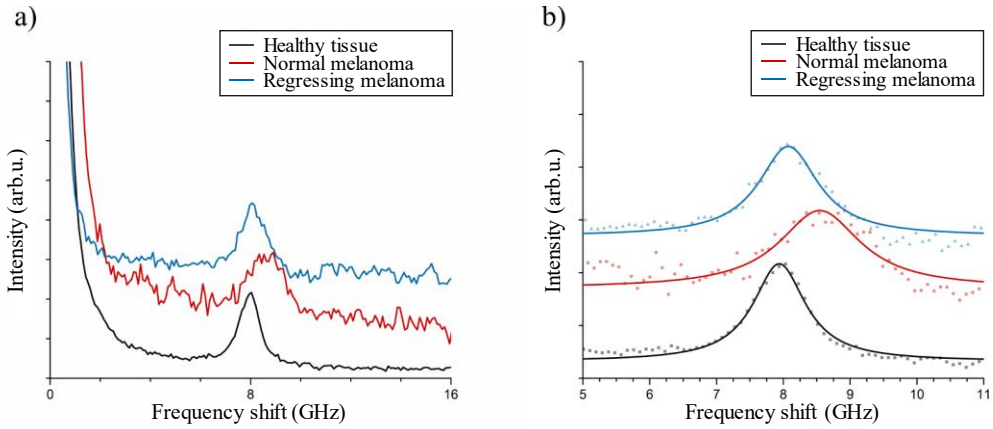

Figure 4.7 Examples of Brillouin spectra, anti-Stokes Brillouin peaks of healthy tissue, normal non-regressing and regressing melanoma: (a) typical raw Brillouin spectra and (b) the expanded view showing the Lorentzian function fit of the data.

One-way ANOVA test was used to compare the means of the Brillouin shift for all samples; the results of the statistical analysis show that the Brillouin shift is significantly different in both melanomas and the surrounding healthy tissue. The average Brillouin shifts are 8.55 ± 0.18 GHz (Normal non-regressing melanoma), 8.11 ± 0.07 GHz (Regressing melanoma), and 7.97 ± 0.02 GHz (Healthy tissue).

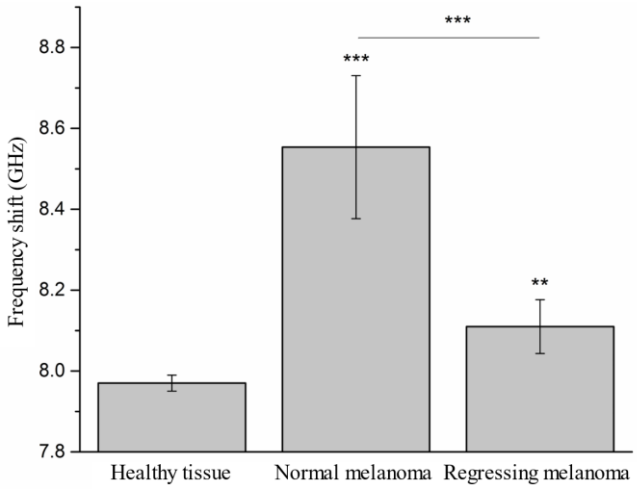

Figure 4.8 Brillouin shifts of the healthy tissue, normal non-regressing and regressing melanomas, displayed as mean ± standard deviation. The difference between the Brillouin shifts is statistically significant (* p≤0.001, ** p≤0.01).**

Both melanoma lesions are stiffer than the surrounding normal tissue, which possesses the smallest value of the Brillouin shift. These results support the literature-based hypothesis that melanoma is stiffer than the healthy tissue. In the present study, the samples included both a non-regressing and a regressing melanoma, and the Brillouin shift shows variation between the two lesion types. The regressing melanoma possesses elasticity closer to that of the surrounding healthy tissue. In Sinclair swine, melanoma regression and loss of pigmentation is related to a rise in antibodies to antigens primarily expressed on melanocytes [42]. Early stage of regression is characterized by a decrease in active melanocytes and predominance of melanophages, while the final stage of regression is histologically similar to normal tissue [132]. The sample used in the present study was at an intermediate stage of regression, with bluish in color lesion and depigmentation halo surrounding it. The reduction in the number of melanocytes and increase in melanin-laden

macrophages and T-lymphocytes at the site likely contribute to the decrease in stiffness of the regressing melanoma compared to the non-regressing melanoma.

The use of the 532-nm wavelength in the present study results in heating of the pigmented tissue due to absorption by melanin. No thermal damage to the sample was observed, however, in order to avoid the damage, the power of the incident radiation was set as low as feasible, which affected the signal to noise ratio of most of our Brillouin spectra. The lower power lead to a longer signal collection time, which, while acceptable for single-point measurements, would be impractical for larger number of data points in point-scanning mode. The present study of elasticity-specific Brillouin measurements of malignant melanoma will be continued, a future study will use Brillouin microspectroscopy to identify melanoma border with high precision by obtaining an elasticity map of the sample. In future studies either a longer incident excitation wavelength, i.e. 780 nm, will be used to reduce the acquisition time, because the skin's absorption and heating generally declines within the 400-1064 nm range as wavelength increases [100,133], or nonlinear Brillouin microscopy measurements [97,134] will be adapted for those tissue measurements.

4.2.4. Conclusion

The ability of Brillouin spectroscopy to differentiate between malignant melanoma and surrounding healthy tissue was successfully demonstrated for the first time. The use of Sinclair miniature swine as an animal model of human malignant melanoma allowed for Brillouin shifts' comparison between the normal non-regressing melanoma, regressing melanoma and the surrounding healthy tissue. The Brillouin shifts of the samples are

statistically significantly different, with the healthy tissue being the softest, and the non-regressing melanoma the stiffest sample.

In the present study, the Brillouin shift of the regressing melanoma differed from the measurements of both the non-regressing melanoma and the heathy tissue. Among the potential applications of Brillouin spectroscopy is not only differentiation between the cancerous and normal tissue, but also monitoring tumor progression or evaluation of treatment efficacy. These potential uses make Brillouin microspectroscopy a valuable tool in cancer research.

Brillouin microspectroscopy is uniquely suitable for distinguishing between different tissues or areas of a sample on the basis of differences in their elastic properties. Brillouin spectroscopy was successfully applied to distinguish between cancerous, regressing and healthy regions of melanoma samples based on their elasticity. This spectroscopic approach shows potential for differentiating malignant melanoma from other pigmented skin lesions, and for finding the boundaries of the lesion with high precision.

4.3 Muscular dystrophy

4.3.1. Introduction

Muscular dystrophy (MD) is a group of muscle diseases, symptoms of which include weakness of skeletal muscles, muscle degeneration and necrosis. Stiffening of the muscles has also been reported [8,135] using various methods. A previous report by our group [136] has illustrated the suitability of using Brillouin spectroscopy to evaluate *ex-vivo* muscular mechanical properties on MD *Drosophila* model expressing homozygous

defects in Protein O-Mannosyltransferase (POMT). Brillouin spectroscopy has been shown to be a powerful tool in a number of biomedical applications [43,52,54–59], and one of its major strengths lies in its ability to perform non-invasive measurements.

In the present study we build upon our previous work that obtained Brillouin spectroscopy measurements of dissected GFP-expressing muscle of POMT Drosophila model [136]. Previous study determined that muscle of POMT mutant larvae possess a higher Brillouin shift than wildtype. We now focus on applying Brillouin spectroscopy in a fully non-invasive fashion in an intact live POMT Drosophila larva without GFP expression. We hypothesize that 1) Brillouin elastography is suitable for non-invasive *in vivo* measurements of larvae muscle mechanical properties, 2) intact muscle of live POMT mutant possess higher Brillouin shift than wild-type and 3) GFP-expression does not affect the stiffness of muscles in either POMT mutant or wildtype group.

4.3.2. Materials and methods

4.3.2.1. Experimental setup

The schematic of the optical system used in the reported study is shown in Figure 4.9. The system can be roughly broken down into 3 sections: Brillouin spectroscopy, Raman spectroscopy and fluorescence imaging measurements.

The excitation light source for simultaneous Brillouin and Raman spectroscopy [42] is a tunable 1064 nm seed laser passing through a MgO:PPLN crystal, resulting in a tunable 532 nm source (as first described in Reference [51]). The offset of the seed laser is set to match a strong absorption band of iodine which serves as an ultra-

narrowband notch filter of elastically scattered light [50]. The incident light is reflected by a polarizing beamsplitter (PBS) cube and is focused onto the sample by a 20x objective.

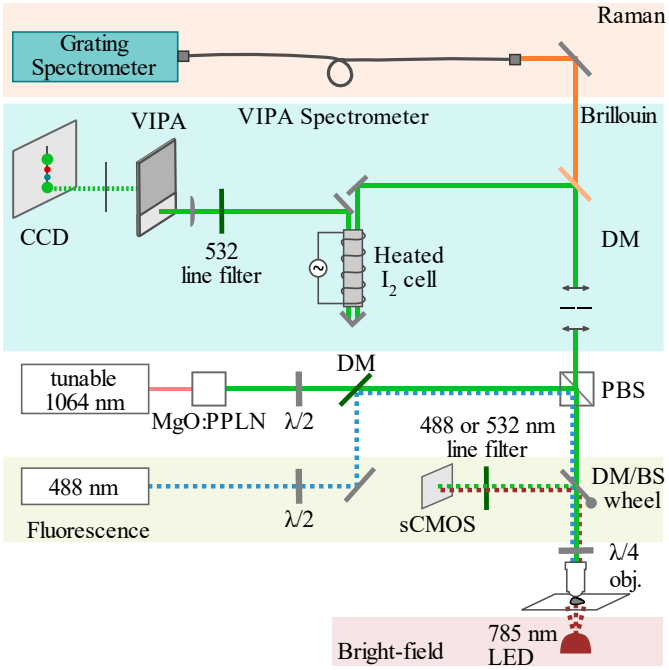

Figure 4.9 Schematic diagram of instrumental setup for Brillouin spectroscopy, features of interest are a tunable 532 nm source (1064 nm seed and SHG crystal), iodine-filled heated cuvette for elastic scattering suppression and VIPA spectrometer.

The collected Brillouin and Raman signal passes through the PBS cube and is separated by the dichroic mirror (532 nm long pass). The Brillouin path consists of 25 μm pinhole to block out-of-focus light, a heated iodine-filled cuvette and VIPA-based spectrometer. The temperature of the iodine-vapor filter is adjusted to ensure sufficient suppression of elastically scattered light without Brillouin peak suppression or baseline distortion (Figure 4.10). The VIPA spectrometer consists of a 100 mm cylindrical lens focusing the beam into an entrance window of the VIPA, and a 1000 mm spherical lens

that focuses the output of the VIPA onto a CCD camera. The Raman spectrometer used in the system is a conventional grating-based spectrometer. The collected Raman spectra are mainly used to facilitate the placement of the larvae and verify that the Brillouin signal is collected from the muscle.

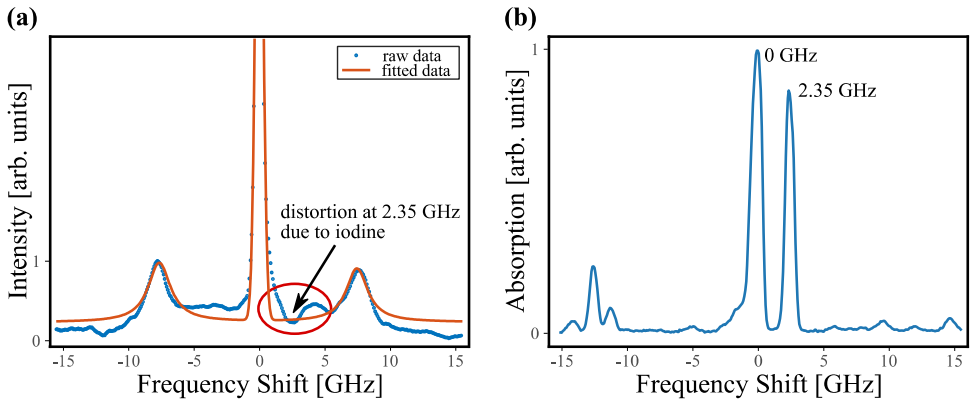

Figure 4.10 a) Brillouin spectrum of *Drosophila* larva muscle, arrow indicates slight baseline distortion caused by iodine absorption. Stronger distortion in highly-scattering samples can affect the Lorentzian fitting of Brillouin peaks. b) Iodine absorption in the region of the excitation wavelength. The smaller band at 2.35 GHz is the cause of the distortion in part a).

The 488 nm excitation light source for the eGFP fluorescence imaging is co-aligned with the 532 nm beam path. A filter wheel placed before the objective has options of a dichroic mirror (515 nm short-pass) for maximum fluorescence collection or 75:25 beamsplitter for simultaneous fluorescence imaging and Brillouin/Raman spectroscopy, as well as a clear window for Brillouin/Raman spectroscopy without fluorescence. A 120mm tube lens focuses the fluorescence image onto a sCMOS with 488 nm line filter for excitation light rejection. The fluorescence imaging was used with eGFP-expressing larvae to train the correct placement of the sample for collection of the Brillouin signal

from the muscle. After the training, the fluorescence imaging was not used for further measurements.

4.3.2.2. POMT *Drosophila* model

Drosophila model of dystroglycanopathies expressing homozygous defects in Protein O-Mannosyltransferase (POMT) genes was utilized in the present study. We performed *in-vivo* measurements from abdominal muscle of third-instar larvae in a total of four experimental groups: wild-type (WT) and POMT mutant (MT), each either with or without eGFP-expression in myosin heavy chain (GFP and noGFP); average n=8 per group.

4.3.2.3. Data analysis

Spectral data were analyzed using custom-written MATLAB code, and the results expressed as mean ± SEM. Data were analyzed using unpaired t-test with a significance value of $\alpha = 0.05$.

The replicate Brillouin spectra for each spatial location were vector normalized and averaged after dark background subtraction. A Lorentzian function fit was used to determine the center pixel position of elastic and Brillouin peaks; the pixel positions were then converted to GHz frequency shifts using polynomial interpolation and the VIPA's free spectral range (FSR) value of 33.34 GHz. The values of Brillouin shift were calculated as the difference between frequencies of each of the Brillouin peaks and the peaks corresponding to the elastically scattered light.

4.3.3. Results and discussion

The results of statistical analysis of the Brillouin spectra are summarized in Figure 4.11, the values are displayed as mean ± SEM. The results indicate that the presence of the GFP protein in the muscle has no effect on its Brillouin shift in either wildtype or POMT mutant larvae. On the other hand, the difference in the muscle's Brillouin shift between control and MD mutant larvae groups is statistically significant ($p<0.05$) for both GFP-expressing and non-expressing larvae. The *in-vivo* measurements show that the muscle of MD mutant displays a higher value of Brillouin shift than the control muscle, which is in agreement with the previous *ex-vivo* study. Notably, the Brillouin shift of the dissected muscle is slightly smaller than that of the intact muscle measured *in-vivo*.

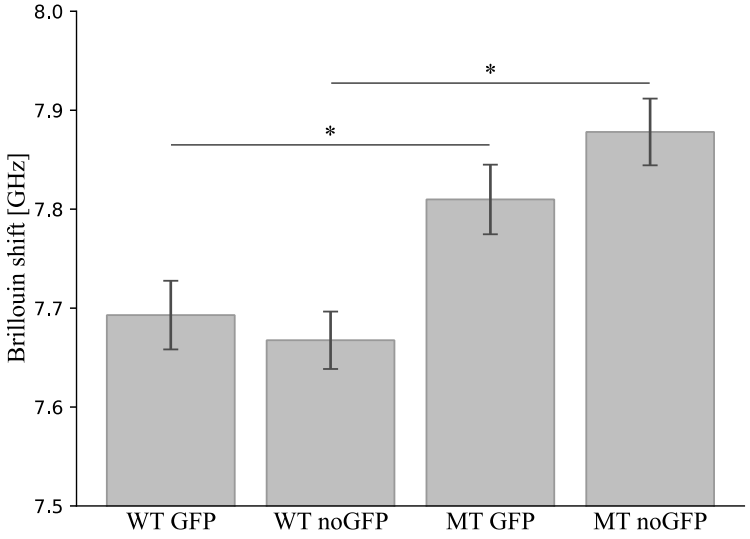

Figure 4.11 The results of statistical analysis of the Brillouin spectra of *Drosophila* larva muscle. There is no statistically significant difference in the Brillouin shift of GFP-expressing and non-expressing muscle of the same group. On the other hand, the difference in the Brillouin shift between corresponding wildtype (WT) and POMT mutant (MT) groups is significant at $\alpha = 0.05$.

4.3.4. Conclusion

In conclusion, we have successfully demonstrated non-invasive Brillouin spectroscopy measurements of POMT and wildtype Drosophila larvae muscle *in-vivo*. We determined that the intact muscle of live POMT mutant possess higher Brillouin shift than wild-type both with and without eGFP expression. Comparison of the results of our current study with the previous work on dissected POMT mutant and wildtype larvae indicates that the intact/*in vivo* muscle possesses a higher Brillouin shift than the dissected muscle. Additionally, we have demonstrated that eGFP expression does not affect the value of the Brillouin shift, therefore is unlikely to affect the mechanical properties of the expressing muscle.

In the present work we have reduced the temperature of the iodine-filled cuvette serving as an ultra-narrow notch filter at the excitation wavelength to balance the suppression of the elastically scattered light and spectrum's SNR. In the future work we will utilize the modification of Brillouin spectroscopy that has been recently developed in our lab, the Sequentially-Shifted Excitation (SSE) Brillouin spectroscopy [61]. SSE Brillouin spectroscopy is a powerful new tool that allows work with highly scattering or fluorescent samples and greatly improves the SNR of the final spectrum. The technique computationally reconstructs the "pure" Brillouin signal component from noisy spectra acquired using 4 or more excitation wavelengths.

5. SUMMARY

In summary, in the scope of the presented dissertation work, a multi-modality experimental system has been implemented that is capable of simultaneous Brillouin elastography, Raman spectroscopy and optional fluorescence widefield or brightfield imaging. The implementation of a tunable 532 nm excitation source provides greater and more reliable suppression of the elastically scattered light. More consistent spectra from measurement to measurement allows for automation of data analysis and use of a reference sample, such as acetone or methanol, to calibrate the VIPA-based spectrometer. Additions of brightfield and fluorescence imaging components aid in positioning the sample to evaluate the region of interest with greater precision.

A novel multi-excitation Brillouin spectroscopy approach was developed to correct for the distortions caused by the excessive iodine absorption, which allows to work with challenging highly-scattering samples. The method provides additional improvement to the SNR of the spectra acquired on systems utilizing molecular absorption filters.

Lastly, the dissertation work includes studies of three different pathologies: obesity, melanoma and muscular dystrophy, showing the application of Brillouin spectroscopy for evaluating mechanical changes in the affected tissues.

REFERENCES

1. C. J. Miller and L. A. Davidson, "The interplay between cell signalling and mechanics in developmental processes.," Nat. Rev. Genet. **14**, 733–744 (2013).
2. L. E. Claes and J. L. Cunningham, "Monitoring the mechanical properties of healing bone.," Clin. Orthop. Relat. Res. **467**, 1964–1971 (2009).
3. H. Gautier, R. Peslin, A. Grassino, J. Milic-Emili, B. Hannhart, E. Powell, G. Miserocchi, M. Bonora, and J. T. Fischer, "Mechanical properties of the lungs during acclimatization to altitude," J. Appl. Physiol. **52**, 1407–1415 (1982).
4. G. Osterhoff, E. F. Morgan, S. J. Shefelbine, L. Karim, L. M. McNamara, and P. Augat, "Bone mechanical properties and changes with osteoporosis.," Injury **47**, S11–S20 (2016).
5. A. E. Peters, R. Akhtar, E. J. Comerford, and K. T. Bates, "The effect of ageing and osteoarthritis on the mechanical properties of cartilage and bone in the human knee joint.," Sci. Rep. **8**, 1–13 (2018).
6. S. Yoon, S. Aglyamov, A. Karpiouk, and S. Emelianov, "The mechanical properties of ex vivo bovine and porcine crystalline lenses: age-related changes and location-dependent variations.," Ultrasound Med. Biol. **39**, 1120–1127 (2013).
7. L. Plantier, A. Cazes, A.-T. Dinh-Xuan, C. Bancal, S. Marchand-Adam, and B. Crestani, "Physiology of the lung in idiopathic pulmonary fibrosis," Eur. Respir. Rev. **27**, 1–14 (2018).
8. L. Lacourpaille, F. Hug, A. Guével, Y. Péréon, A. Magot, J.-Y. Hogrel, and A.

Nordez, "Non-invasive assessment of muscle stiffness in patients with Duchenne muscular dystrophy," Muscle and Nerve **51**, 284–286 (2015).

9. S. F. Bensamoun, F. Charleux, L. Debernard, C. Themar-Noel, and T. Voit, "Elastic properties of skeletal muscle and subcutaneous tissues in Duchenne muscular dystrophy by magnetic resonance elastography (MRE): A feasibility study," IRBM **36**, 4–9 (2015).

10. A. Itoh, E. Ueno, E. Tohno, H. Kamma, H. Takahashi, T. Shiina, M. Yamakawa, and T. Matsumura, "Breast disease: clinical application of US elastography for diagnosis.," Radiology **239**, 341–350 (2006).

11. D. T. Ginat, S. V Destounis, R. G. Barr, B. Castaneda, J. G. Strang, and D. J. Rubens, "US elastography of breast and prostate lesions.," Radiographics **29**, 2007–2016 (2009).

12. C. M. Botar-Jid, R. Cosgarea, S. D. Bolboacă, S. C. Şenilă, L. M. Lenghel, L. Rogojan, and S. M. Dudea, "Assessment of cutaneous melanoma by use of very-high-frequency ultrasound and real-time elastography," Am. J. Roentgenol. 1–6 (2016).

13. G. Low, S. A. Kruse, and D. J. Lomas, "General review of magnetic resonance elastography.," World J. Radiol. **8**, 59–72 (2016).

14. J. Ophir, I. Céspedes, H. Ponnekanti, Y. Yazdi, and X. Li, "Elastography: A quantitative method for imaging the elasticity of biological tissues," Ultrason. Imaging **13**, 111–134 (1991).

15. C. Passmann and H. Ermert, "A 100-MHz ultrasound imaging system for

dermatologic and ophthalmologic diagnostics," IEEE Trans. Ultrason. Ferroelectr. Freq. Control **43**, 545–552 (1996).

16. S. Wang and K. V. Larin, "Optical coherence elastography for tissue characterization: a review," J. Biophotonics **8**, 279–302 (2015).
17. K. V. Larin and D. D. Sampson, "Optical coherence elastography – OCT at work in tissue biomechanics [Invited]," Biomed. Opt. Express **8**, 1172–1202 (2017).
18. P. Hai, J. Yao, G. Li, C. Li, and L. V. Wang, "Photoacoustic elastography," Opt. Lett. **41**, 725–728 (2016).
19. M. S. Singh and A. Thomas, "Photoacoustic elastography imaging: a review," J. Biomed. Opt. **24**, 1--15 (2019).
20. K. D. Costa, "Single-cell elastography: probing for disease with the atomic force microscope.," Dis. Markers **19**, 139–154 (2004).
21. M. J. Paszek, N. Zahir, K. R. Johnson, J. N. Lakins, G. I. Rozenberg, A. Gefen, C. A. Reinhart-King, S. S. Margulies, M. Dembo, D. Boettiger, D. A. Hammer, and V. M. Weaver, "Tensional homeostasis and the malignant phenotype," Cancer Cell **8**, 241–254 (2005).
22. A. Stylianou and T. Stylianopoulos, "Atomic force microscopy probing of cancer cells and tumor microenvironment components," Bionanoscience **2016**, 33–46 (2015).
23. S. Kumar and V. M. Weaver, "Mechanics, malignancy, and metastasis: The force journey of a tumor cell," Cancer Metastasis Rev. **28**, 113–127 (2009).
24. J. M. Tse, G. Cheng, J. A. Tyrrell, S. A. Wilcox-Adelman, Y. Boucher, R. K. Jain,

and L. L. Munn, "Mechanical compression drives cancer cells toward invasive phenotype.," Proc. Natl. Acad. Sci. U. S. A. **109**, 911–916 (2012).

25. M. Lekka, K. Pogoda, J. Gostek, O. Klymenko, S. Prauzner-Bechcicki, J. Wiltowska-Zuber, J. Jaczewska, J. Lekki, and Z. Stachura, "Cancer cell recognition - Mechanical phenotype," Micron **43**, 1259–1266 (2012).

26. V. Swaminathan, K. Mythreye, E. T. O'Brien, A. Berchuck, G. C. Blobe, and R. Superfine, "Mechanical stiffness grades metastatic potential in patient tumor cells and in cancer cell lines," Cancer Res. **71**, 5075–5080 (2011).

27. G. Weder, M. C. Hendriks-Balk, R. Smajda, D. Rimoldi, M. Liley, H. Heinzelmann, A. Meister, and A. Mariotti, "Increased plasticity of the stiffness of melanoma cells correlates with their acquisition of metastatic properties," Nanomedicine Nanotechnology, Biol. Med. **10**, 141–148 (2014).

28. G. Antonacci, M. R. Foreman, C. Paterson, and P. Török, "Spectral broadening in Brillouin imaging," Appl. Phys. Lett. **103**, 1–4 (2013).

29. R. Vacher and L. Boyer, "Brillouin scattering: a tool for the measurement of elastic and photoelastic constants," Phys. Rev. B **6**, 639–673 (1972).

30. M. H. Manghnani, X. Zhang, S. Tkachev, P. Zinin, H. Feldermann, C. Ronning, H. Hofsäss, and A. G. Every, "Elastic properties of cBN films by surface Brillouin scattering," AIP Conf. Proc. **497**, 315–320 (1999).

31. E. S. Fry, Y. Emery, X. Quan, and J. W. Katz, "Accuracy limitations on Brillouin lidar measurements of temperature and sound speed in the ocean," Appl. Opt. **36**, 6887–6894 (1997).

32. G. Scarcelli, R. Pineda, and S. Yun, "Brillouin optical microscopy for corneal biomechanics," Invest. Ophthalmol. Vis. Sci. **53**, 185–190 (2012).

33. S. Reiß, G. Burau, and O. Stachs, "Spatially resolved Brillouin spectroscopy to determine the rheological properties of the eye lens," Biomed. Opt. Express **2**, 2144–2159 (2011).

34. Z. Steelman, Z. Meng, A. J. Traverso, and V. V. Yakovlev, "Brillouin spectroscopy as a new method of screening for increased CSF total protein during bacterial meningitis," J. Biophotonics **8**, 408–414 (2015).

35. J. P. Lepesant, L. Powers, and P. S. Pershan, "Brillouin light scattering measurement of the elastic properties of aligned multilamella lipid samples," Proc. Natl. Acad. Sci. U. S. A. **75**, 1792–1795 (1978).

36. G. Scarcelli, W. J. Polacheck, H. T. Nia, K. Patel, A. J. Grodzinsky, R. D. Kamm, and S. H. Yun, "Noncontact three-dimensional mapping of intracellular hydromechanical properties by Brillouin microscopy," Nat. Methods **12**, 1132–1134 (2015).

37. Z. Meng, S. C. Bustamante Lopez, K. E. Meissner, and V. V. Yakovlev, "Subcellular measurements of mechanical and chemical properties using dual Raman-Brillouin microspectroscopy," J. Biophotonics **9**, 201–207 (2015).

38. J. M. Vaughan and J. T. Randall, "Brillouin scattering, density and elastic properties of the lens and cornea of the eye," Nature **284**, 489–491 (1980).

39. G. Scarcelli and S. H. Yun, "Multistage VIPA etalons for high-extinction parallel Brillouin spectroscopy.," Opt. Express **19**, 10913–10922 (2011).

40. P. Shao, S. Besner, J. Zhang, G. Scarcelli, and S.-H. Yun, "Etalon filters for Brillouin microscopy of highly scattering tissues," Opt. Express **24**, 22232–22238 (2016).

41. A. Fiore, J. Zhang, P. Shao, S. H. Yun, and G. Scarcelli, "High-extinction virtually imaged phased array-based Brillouin spectroscopy of turbid biological media," Appl. Phys. Lett. **108**, 2–5 (2016).

42. A. J. Traverso, J. V. Thompson, Z. A. Steelman, Z. Meng, M. O. Scully, and V. V. Yakovlev, "Dual Raman-Brillouin microscope for chemical and mechanical characterization and imaging," Anal. Chem. **87**, 7519–7523 (2015).

43. M. Troyanova-Wood, C. Gobbell, Z. Meng, A. A. Gashev, and V. V. Yakovlev, "Optical assessment of changes in mechanical and chemical properties of adipose tissue in diet-induced obese rats," J. Biophotonics **10**, 1694–1702 (2017).

44. K. J. Koski and J. L. Yarger, "Brillouin imaging," Appl. Phys. Lett. **87**, 1–3 (2005).

45. M. Shirasaki, "Large angular dispersion by a virtually imaged phased array and its application to a wavelength demultiplexer.," Opt. Lett. **21**, 366–368 (1996).

46. V. M. Shirasaki, "Virtually imaged phased array," Fujitsu Sci. Tech. J. **35**, 113–125 (1999).

47. J. D. Simmons and J. T. Hougen, "Atlas of the I_2 Spectrum from 19 000 to 18 000 cm^{-1}," J. Res. Natl. Bur. Stand. Sect. A Phys. Chem. **81A**, 25–80 (1977).

48. S. Xiao, A. M. Weiner, and C. Lin, "A dispersion law for virtually imaged phased-array spectral dispersers based on paraxial wave theory," IEEE J. Quantum Electron. **40**, 420–426 (2004).

49. Z. Meng, "Non-destructive viscoelasticity microscopy: a spectroscopic approach using dual Brillouin/Raman scattering processes," Ph.D. Dissertation, Texas A&M University, College Station,TX (2016).

50. Z. Meng, A. J. Traverso, and V. V Yakovlev, "Background clean-up in Brillouin microspectroscopy of scattering medium," Opt. Express **22**, 5410–5415 (2014).

51. Z. Coker, M. Troyanova-Wood, A. J. Traverso, T. Yakupov, Z. N. Utegulov, and V. V Yakovlev, "Assessing performance of modern Brillouin spectrometers," Opt. Express **26**, 2400–2409 (2018).

52. Z. Meng, A. J. Traverso, C. W. Ballmann, M. A. Troyanova-Wood, and V. V. Yakovlev, "Seeing cells in a new light: a renaissance of Brillouin spectroscopy," Adv. Opt. Photonics **8**, 300–327 (2016).

53. V. V. Yakovlev, C. W. Ballmann, Z. Coker, Z. Meng, and M. Troyanova-Wood, "What is next for Brillouin microscopy in biology and medicine?," Proc. SPIE **10067**, 100670J.1-6 (2017).

54. O. Y. Gasheva, I. T. Nizamutdinova, L. Hargrove, C. Gobbell, M. Troyanova-Wood, S. F. Alpini, S. Pal, C. Du, A. R. Hitt, V. V Yakovlev, M. K. Newell-Rogers, D. C. Zawieja, C. J. Meininger, G. D. Alpini, H. Francis, and A. A. Gashev, "Prolonged intake of desloratadine : mesenteric lymphatic vessel dysfunction and development of obesity / metabolic syndrome," Am. J. Physiol. Liver Physiol. **316**, 217–227 (2019).

55. P.-J. Wu, I. V. Kabakova, R. W. Jeffrey, J. M. Sherwood, I. E. Dunlop, C. Paterson, P. Török, and D. R. Overby, "Water content, not stiffness, dominates Brillouin

spectroscopy measurements in hydrated materials," Nat. Methods **15**, 561–562 (2018).

56. K. Elsayad, S. Werner, M. Gallemí, J. Kong, E. R. S. Guajardo, L. Zhang, Y. Jaillais, T. Greb, and Y. Belkhadir, "Mapping the subcellular mechanical properties of live cells in tissues with fluorescence emission-Brillouin imaging," Sci. Signal. **9**, 1–13 (2016).

57. J. Zhang, A. Fiore, S. H. Yun, H. Kim, and G. Scarcelli, "Line-scanning Brillouin microscopy for rapid non-invasive mechanical imaging," Sci. Rep. **6**, 1–8 (2016).

58. F. Palombo, M. Madami, D. Fioretto, J. Nallala, H. Barr, A. David, and N. Stone, "Chemico-mechanical imaging of Barrett's oesophagus," J. Biophotonics **9**, 694–700 (2016).

59. M. Troyanova-Wood, Z. Meng, and V. V. Yakovlev, "Differentiating melanoma and healthy tissues based on elasticity-specific Brillouin microspectroscopy," Biomed. Opt. Express **10**, 1774–1781 (2019).

60. D. Akilbekova, V. Ogay, T. Yakupov, M. Sarsenova, B. Umbayev, A. Nurakhmetov, K. Tazhin, V. V. Yakovlev, and Z. N. Utegulov, "Brillouin spectroscopy and radiography for assessment of viscoelastic and regenerative properties of mammalian bones," J. Biomed. Opt. **23**, 097004.1-11 (2018).

61. M. Troyanova-Wood and V. V. Yakovlev, "Sequentially-shifted excitation (SSE) Brillouin spectroscopy for recovering signal contaminated with strong scattering, absorption or fluorescence," Proc. SPIE **10880**, 1088016.1-6 (2019).

62. G. Schulze, A. Jirasek, M. M. L. Yu, A. Lim, R. F. B. Turner, and M. W. Blades,

"Investigation of selected baseline removal techniques as candidates for automated implementation," Appl. Spectrosc. **59**, 545–574 (2005).

63. S. T. McCain, R. M. Willett, and D. J. Brady, "Multi-excitation Raman spectroscopy technique for fluorescence rejection," Opt. Express **16**, 10975–10991 (2008).

64. J. B. Cooper, M. Abdelkader, and K. L. Wise, "Sequentially shifted excitation Raman spectroscopy: Novel algorithm and instrumentation for fluorescence-free Raman spectroscopy in spectral space," Appl. Spectrosc. **67**, 973–984 (2013).

65. World Health Organization, *Fact Sheet 311: Obesity and Overweight* (2016).

66. P. G. Kopelman, "Obesity as a medical problem," Nature **404**, 635–643 (2000).

67. A. Must, J. Spadano, E. H. Coakley, A. E. Field, G. Colditz, and W. H. Dietz, "The disease burden associated with overweight and obesity," JAMA **282**, 1523–1529 (1999).

68. G. Martinez-Santibañez and C. N. Lumeng, "Macrophages and the regulation of adipose tissue remodeling," Annu. Rev. Nutr. **34**, 57–76 (2014).

69. E. C. M. Mariman and P. Wang, "Adipocyte extracellular matrix composition, dynamics and role in obesity," Cell. Mol. Life Sci. **67**, 1277–1292 (2010).

70. N. Shoham, P. Girshovitz, R. Katzengold, N. T. Shaked, D. Benayahu, and A. Gefen, "Adipocyte stiffness increases with accumulation of lipid droplets," Biophys. J. **106**, 1421–1431 (2014).

71. N. Alkhouli, J. Mansfield, E. Green, J. Bell, B. Knight, N. Liversedge, J. C. Tham, R. Welbourn, A. C. Shore, K. Kos, and C. P. Winlove, "The mechanical properties

of human adipose tissues and their relationships to the structure and composition of the extracellular matrix," Am. J. Physiol. - Endocrinol. Metab. **305**, 1427–1435 (2013).

72. V. Pellegrinelli, J. Heuvingh, O. du Roure, C. Rouault, A. Devulder, C. Klein, M. Lacasa, E. Clément, D. Lacasa, and K. Clément, "Human adipocyte function is impacted by mechanical cues," J. Pathol. **233**, 183–195 (2014).

73. N. Shoham and A. Gefen, "Mechanotransduction in adipocytes," J. Biomech. **45**, 1–8 (2012).

74. N. Shoham and A. Gefen, "The biomechanics of fat: From tissue to a cell scale," in *Structure-Based Mechanics of Tissues and Organs* (Springer; Boston, MA, 2016), pp. 79–92.

75. R. Boyd, *Nonlinear Optics* (Academic Press; San Diego, CA, 2003).

76. M. Troyanova-Wood, Z. Meng, and V. V Yakovlev, "Elasticity-based identification of tumor margins using Brillouin spectroscopy," Prog. Biomed. Opt. Imaging - Proc. SPIE **9719**, 97190P.1-6 (2016).

77. M. Abdennour, S. Reggio, G. Le Naour, Y. Liu, C. Poitou, J. Aron-wisnewsky, F. Charlotte, J. Bouillot, A. Torcivia, M. Sasso, V. Miette, J. Zucker, P. Bedossa, J. Tordjman, and K. Clement, "Association of adipose tissue and liver fibrosis with tissue stiffness in morbid obesity : Links with diabetes and BMI loss after gastric bypass," J. Clin. Endocrinol. Metab. **99**, 898–907 (2014).

78. M. Giarola, B. Rossi, E. Mosconi, M. Fontanella, P. Marzola, I. Scambi, A. Sbarbati, and G. Mariotto, "Fast and minimally invasive determination of the

unsaturation index of white fat depots by micro-Raman spectroscopy.," Lipids **46**, 659–67 (2011).

79. M. Giarola, G. Guella, G. Mariotto, F. Monti, B. Rossi, A. Sanson, and A. Sbarbati, "Vibrational and structural investigations on adipose tissues," Philos. Mag. **88**, 3953–3959 (2008).

80. M. N. Alahbabi, Y. T. Cho, and T. P. Newson, "Simultaneous temperature and strain measurement with combined spontaneous Raman and Brillouin scattering," Opt. Lett. **30**, 1276–1278 (2005).

81. G. Bolognini, M. A. Soto, and F. D. Pasquale, "Simultaneous distributed strain and temperature sensing based on combined Raman-Brillouin scattering using Fabry-Perot lasers," Meas. Sci. Technol. **21**, 1–8 (2010).

82. C. H. Saely, K. Geiger, and H. Drexel, "Brown versus white adipose tissue: A mini-review," Gerontology **58**, 15–23 (2011).

83. Z. Meng and V. V. Yakovlev, "Optimizing signal collection efficiency of the VIPA-based Brillouin spectrometer," J. Innov. Opt. Health Sci. **8**, 1550021.1-7 (2015).

84. Z. Meng and V. V. Yakovlev, "Precise determination of Brillouin scattering spectrum using a virtually imaged phase array (VIPA) spectrometer and charge-coupled device (CCD) camera," Appl. Spectrosc. **70**, 1356–1363 (2016).

85. G. Scarcelli and S. Yun, "Confocal Brillouin microscopy for three-dimensional mechanical imaging," Nat. Photonics **2**, 39–43 (2008).

86. A. C. S. Talari, Z. Movasaghi, S. Rehman, and I. U. Rehman, "Raman spectroscopy of biological tissues," Appl. Spectrosc. Rev. **50**, 46–111 (2015).

87. F. P. Bolin, L. E. Preuss, R. C. Taylor, and R. J. Ference, "Refractive index of some mammalian tissues using a fiber cladding method.," **28**, 2297–2303 (1989).

88. F. Duck, *Physical Properties of Tissue : A Comprehensive Reference Book* (Academic Press; San Diego, CA, 1990).

89. A. Divoux, J. Tordjman, D. Lacasa, N. Veyrie, D. Hugol, A. Aissat, A. Basdevant, M. Guerre-Millo, C. Poitou, J.-D. Zucker, P. Bedossa, and K. Clément, "Fibrosis in human adipose tissue : Composition, distribution, and link with lipid metabolism and fat," Diabetes **59**, 2817–2825 (2010).

90. T. Khan, E. S. Muise, P. Iyengar, Z. V. Wang, M. Chandalia, N. Abate, B. B. Zhang, P. Bonaldo, S. Chua, and P. E. Scherer, "Metabolic dysregulation and adipose tissue fibrosis : Role of collagen VI," Mol. Cell. Biol. **29**, 1575–1591 (2009).

91. K. J. Strissel, Z. Stancheva, H. Miyoshi, J. W. Perfield, J. DeFuria, Z. Jick, A. S. Greenberg, and M. S. Obin, "Adipocyte death, adipose tissue remodeling, and obesity complications," Diabetes **56**, 2910–2918 (2007).

92. S. P. Weisberg, D. McCann, M. Desai, M. Rosenbaum, R. L. Leibel, and A. W. Ferrante, "Obesity is associated with macrophage accumulation in adipose tissue," J. Clin. Invest. **112**, 1796–1808 (2003).

93. D. Medrikova, Z. M. Jilkova, K. Bardova, P. Janovska, M. Rossmeisl, and J. Kopecky, "Sex differences during the course of diet-induced obesity in mice: adipose tissue expandability and glycemic control," Int. J. Obes. **36**, 262–272 (2012).

94. G. I. Petrov, Z. Meng, and V. V. Yakovlev, "Electronically tunable coherent Raman

spectroscopy using acousto-optics tunable filter," Opt. Express **23**, 24669–24674 (2015).

95. Z. Meng, G. I. Petrov, and V. V. Yakovlev, "Pure electrical, highly-efficient and sidelobe free coherent Raman spectroscopy using acousto-optics tunable filter (AOTF)," Sci. Rep. **6**, 1–7 (2016).

96. C. W. Ballmann, J. V Thompson, A. J. Traverso, Z. Meng, M. O. Scully, and V. V Yakovlev, "Stimulated Brillouin scattering microscopic imaging," Sci. Rep. **5**, (2015).

97. Z. Meng, G. I. Petrov, and V. V Yakovlev, "Flow cytometry using Brillouin imaging and sensing via time-resolved optical (BISTRO) measurements," Analyst **140**, 7160–7164 (2015).

98. R. Arora, G. I. Petrov, V. V Yakovlev, and M. O. Scully, "Chemical analysis of molecular species through turbid medium," Anal. Chem. **86**, 1445-1451 (2013).

99. V. V. Yakovlev, "Advanced instrumentation for non-linear Raman microscopy," J. Raman Spectrosc. **34**, 957–964 (2003).

100. J. N. Bixler, B. H. Hokr, M. L. Denton, G. D. Noojin, D. Aurora, H. T. Beier, R. J. Thomas, B. A. Rockwell, and V. V. Yakovlev, "Assessment of tissue heating under tunable near IR radiation," J. Biomed. Opt. **19**, (2015).

101. A. J. Miller and M. C. J. Mihm, "Melanoma," N. Engl. J. Med. **355**, 51–65 (2006).

102. C. Garbe and U. Leiter, "Melanoma epidemiology and trends," Clin. Dermatol. **27**, 3–9 (2009).

103. American Cancer Society, "American Cancer Society: Cancer Facts and Figures

2015," (2015).

104. C. M. Grin, A. Kopf, B. Welkovich, R. S. Bart, and M. J. Levenstein, "Accuracy in the clinical diagnosis of malignant melanoma," Arch. Dermatol. **126**, 763–766 (1990).

105. G. Argenziano and H. P. Soyer, "Dermoscopy of pigmented skin lesions – a valuable tool for early diagnosis of melanoma," Lancet **2**, 443–449 (2001).

106. H. Kittler, H. Pehamberger, K. Wolff, and M. Binder, "Diagnostic accuracy of dermoscopy," Lancet Oncol. **3**, 159–165 (2002).

107. K. Hoffmann, J. Jung, S. el Gammal, and P. Altmeyer, "Malignant melanoma in 20-MHz B scan sonography," Dermatology **185**, 49–55 (1992).

108. C. C. Harland, S. G. Kale, P. Jackson, P. S. Mortimer, and J. C. Bamber, "Differentiation of common benign pigmented skin lesions from melanoma by high-resolution ultrasound," Br. J. Dermatol. **143**, 281–289 (2000).

109. C. Botar-Jid, S. D. Bolboacă, R. Cosgarea, S. Şenilă, L. Rogojan, M. Lenghel, D. Vasilescu, and S. M. Dudea, "Doppler ultrasound and strain elastography in the assessment of cutaneous melanoma: Preliminary results," Med. Ultrason. **17**, 509–514 (2015).

110. T. Hinz, J. Wenzel, and M.-H. Schmid-Wendtner, "Real-time tissue elastography: a helpful tool in the diagnosis of cutaneous melanoma?," J. Am. Acad. Dermatol. **65**, 424–426 (2011).

111. M. Elbaum, A. W. Kopf, H. S. Rabinovitz, R. G. Langley, H. Kamino, M. C. Mihm, A. J. Sober, G. L. Peck, A. Bogdan, D. Gutkowicz-Krusin, M. Greenebaum, S.

Keem, M. Oliviero, and S. Wang, "Automatic differentiation of melanoma from melanocytic nevi with multispectral digital dermoscopy: a feasibility study.," J. Am. Acad. Dermatol. **44**, 207–218 (2001).

112. S. Tomatis, M. Carrara, A. Bono, C. Bartoli, M. Lualdi, G. Tragni, A. Colombo, and R. Marchesini, "Automated melanoma detection with a novel multispectral imaging system: results of a prospective study.," Phys. Med. Biol. **50**, 1675–1687 (2005).

113. I. Diebele, I. Kuzmina, A. Lihachev, J. Kapostinsh, A. Derjabo, L. Valeine, and J. Spigulis, "Clinical evaluation of melanomas and common nevi by spectral imaging.," Biomed. Opt. Express **3**, 467–472 (2012).

114. A. Premkumar, F. Marincola, J. Taubenberger, C. Chow, D. Venzon, and D. Schwartzentruber, "Metastatic melanoma: Correlation of MRI characteristics and histopathology," J. Magn. Reson. Imaging **6**, 190–194 (1996).

115. H. Yoshioka, T. Kamada, S. Kandatsu, M. Koga, K. Yoshikawa, Y. Matsuoka, J. Mizoe, Y. Itai, and H. Tsujii, "MRI of mucosal malignant melanoma of the head and neck," J. Comput. Assist. Tomogr. **22**, 492–497 (1998).

116. S. Sigurdsson, P. A. Philipsen, L. K. Hansen, J. Larsen, M. Gniadecka, and H. C. Wulf, "Detection of skin cancer by classification of Raman spectra," IEEE Trans. Biomed. Eng. **51**, 1784–1793 (2004).

117. C. A. Lieber, S. K. Majumder, D. Billheimer, D. L. Ellis, and A. Mahadevan-Jansen, "Raman microspectroscopy for skin cancer detection in vitro.," J. Biomed. Opt. **13**, 024013.1-9 (2008).

118. H. Lui, J. Zhao, D. McLean, and H. Zeng, "Real-time Raman spectroscopy for in vivo skin cancer diagnosis," Cancer Res. **72**, 2491–2500 (2012).

119. L. Provencher, J. C. Hogue, C. Desbiens, B. Poirier, E. Poirier, D. Boudreau, M. Joyal, C. Diorio, N. Duchesne, and J. Chiquette, "Is clinical breast examination important for breast cancer detection ?," **23**, 332–339 (2016).

120. J. Guck, S. Schinkinger, B. Lincoln, F. Wottawah, S. Ebert, M. Romeyke, D. Lenz, H. M. Erickson, R. Ananthakrishnan, D. Mitchell, J. Käs, S. Ulvick, and C. Bilby, "Optical deformability as an inherent cell marker for testing malignant transformation and metastatic competence," Biophys. J. **88**, 3689–3698 (2005).

121. T. Krouskop, T. Wheeler, and F. Kallel, "Elastic moduli of breast and prostate tissues under compression," Ultrason. Imaging **20**, 260–274 (1998).

122. P. Wellman, R. D. Howe, E. Dalton, and K. A. Kern, *Breast Tissue Stiffness in Compression Is Correlated to Histological Diagnosis* (Harvard, Cambridge, MA, 1999).

123. S. E. Cross, Y.-S. Jin, J. Rao, and J. K. Gimzewski, "Nanomechanical analysis of cells from cancer patients.," Nat. Nanotechnol. **2**, 780–783 (2007).

124. S. Suresh, "Nanomedicine: Elastic clues in cancer detection.," Nat. Nanotechnol. **2**, 748–749 (2007).

125. M. Sarna, A. Zadlo, A. Pilat, M. Olchawa, P. Gkogkolou, K. Burda, M. Böhm, and T. Sarna, "Nanomechanical analysis of pigmented human melanoma cells," Pigment Cell Melanoma Res. **26**, 727–730 (2013).

126. S. Mattana, M. Mattarelli, L. Urbanelli, K. Sagini, C. Emiliani, M. D. Serra, D.

Fioretto, and S. Caponi, "Non-contact mechanical and chemical analysis of single living cells by microspectroscopic techniques," Light Sci. Appl. **7**, 1–9 (2018).

127. R. Schlüßler, S. Möllmert, S. Abuhattum, G. Cojoc, P. Müller, K. Kim, C. Möckel, C. Zimmermann, J. Czarske, and J. Guck, "Mechanical mapping of spinal cord growth and repair in living zebrafish larvae by Brillouin imaging," Biophys. J. **115**, 911–923 (2018).

128. S. Mattana, S. Caponi, F. Tamagnini, D. Fioretto, and F. Palombo, "Viscoelasticity of amyloid plaques in transgenic mouse brain studied by Brillouin microspectroscopy and correlative Raman analysis," J. Innov. Opt. Health Sci. **10**, 1742001.1-14 (2017).

129. G. Antonacci and S. Braakman, "Biomechanics of subcellular structures by non-invasive Brillouin microscopy," Sci. Rep. **6**, 1–7 (2016).

130. G. S. Figueiredo, S. Bojic, P. Rooney, S. P. Wilshaw, C. J. Connon, R. M. Gouveia, C. Paterson, G. Lepert, H. S. Mudhar, F. C. Figueiredo, and M. Lako, "Gamma-irradiated human amniotic membrane decellularised with sodium dodecyl sulfate is a more efficient substrate for the ex vivo expansion of limbal stem cells," Acta Biomater. **61**, 124–133 (2017).

131. J. N. Webb, J. P. Su, and G. Scarcelli, "Mechanical outcome of accelerated corneal crosslinking evaluated by Brillouin microscopy," J. Cataract Refract. Surg. **43**, 1458–1463 (2017).

132. L. E. Millikan, J. L. Boylon, R. R. Hook, and P. J. Manning, "Melanoma in Sinclair swine : a new animal model," J. Invest. Dermatol. **62**, 20–30 (1974).

133. E. Salomatina, B. Jiang, J. Novak, and A. N. Yaroslavsky, "Optical properties of normal and cancerous human skin in the visible and near-infrared spectral range," J. Biomed. Opt. **11**, 064026.1-9 (2006).

134. C. W. Ballmann, Z. Meng, A. J. Traverso, V. V Yakovlev, and M. O. Scully, "Impulsive Brillouin microscopy," Optica **4**, 124–128 (2017).

135. A. Berquin, P. Schmit, P. Moens, and J. Lebacq, "Compliance of normal, dystrophic and transplanted mouse muscles," J. Biomech. **27**, 1331–1337 (1994).

136. Z. Meng, R. Baker, V. M. Panin, and V. V. Yakovlev, "Brillouin spectroscopy reveals changes in muscular viscoelasticity in Drosophila POMT mutants," Proc. SPIE **9327**, 932713.1-7 (2015).